

1 **Title**

2 Carotenoid assembly regulates quinone diffusion and the *Roseiflexus castenholzii* reaction center-
3 light harvesting complex architecture

4 **Authors**

5 Jiyu Xin,^{1#} Yang Shi,^{2#} Xin Zhang,^{1,3#} Xinyi Yuan,^{1,3} Yueyong Xin,³ Huimin He,³ Jiejie Shen,¹
6 Robert E. Blankenship,⁴ Xiaoling Xu,^{1,2*}

7

8 **Affiliations**

9 ¹Department of Biochemistry and Molecular Biology, School of Basic Medical Sciences and The
10 Affiliated Hospital of Hangzhou Normal University, Hangzhou, 311121, China

11 ²Liangzhu Laboratory, MOE Frontier Science Center for Brain Science and Brain-machine
12 Integration, State Key Laboratory of Brain-machine Intelligence & Department of Neurobiology
13 and Department of Pathology of the First Affiliated Hospital, Zhejiang University School of
14 Medicine, Zhejiang University, Hangzhou, 311121, China

15 ³Photosynthesis Research Center, College of Life and Environmental Sciences, Hangzhou Normal
16 University, Hangzhou, 311121, China

17 ⁴Departments of Biology and Chemistry, Washington University in St. Louis, St. Louis, MO
18 63130, USA

19

20 # These authors contributed equally to this work.

21 *Correspondence should be addressed to Xiaoling Xu. (xuxl@hznu.edu.cn)

22

23

24

25

26 **Abstract**

27 Carotenoid (Car) pigments perform central roles in photosynthesis-related light harvesting (LH),
28 photoprotection, and assembly of functional pigment-protein complexes. However, the
29 relationships between Car depletion in the LH, assembly of the prokaryotic reaction center (RC)-
30 LH complex, and quinone exchange are not fully understood. Here, we analyzed native RC-LH
31 (nRC-LH) and Car-depleted RC-LH (dRC-LH) complexes in *Roseiflexus castenholzii*, a
32 chlorosome-less filamentous anoxygenic phototroph that forms the deepest branch of
33 photosynthetic bacteria. Newly identified exterior Cars functioned with the bacteriochlorophyll
34 B800 to block the proposed quinone channel between LH $\alpha\beta$ subunits in the nRC-LH, forming a
35 sealed LH ring that was disrupted by transmembrane helices from cytochrome c and subunit X to
36 allow quinone shuttling. dRC-LH lacked subunit X, leading to an exposed LH ring with a larger
37 opening, which together accelerated the quinone exchange rate. We also assigned amino acid
38 sequences of subunit X and two hypothetical proteins Y and Z that functioned in forming the
39 quinone channel and stabilizing the RC-LH interactions. This study reveals the structural basis by
40 which Cars assembly regulates the architecture and quinone exchange of bacterial RC-LH
41 complexes. These findings mark an important step forward in understanding the evolution and
42 diversity of prokaryotic photosynthetic apparatus.

43

44

45 **Introduction**

46 Carotenoids (Cars) are natural pigments that play important roles in light harvesting,
47 photoprotection, and assembly of the functional pigment-protein complexes required for
48 photosynthesis. Specifically, Cars capture blue-green light (450-550 nm) and transfer it to
49 chlorophyll or bacteriochlorophyll ((B)Chl) in the light-harvesting (LH) antenna. The excited
50 energy is then transferred to the reaction center (RC) for primary photochemical reactions. In

51 anoxygenic photosynthetic bacteria (PSB), Car-BChl interactions are essential for assembling the
52 functional LH complexes (Davidson & Cogdell, 1981; Hashimoto, Uragami, & Cogdell, 2016; H.
53 Lang & Hunter, 1994; Walz & Ghosh, 1997). The well-studied purple bacterium *Rhodobacter*
54 (*Rba.*) *sphaeroides* contains a closed LH2 ring comprising nine $\alpha\beta$ -polypeptides; each LH $\alpha\beta$
55 noncovalently binds three BChls (two B850s and one B800) and one Car (Qian, Swainsbury,
56 Croll, Castro-Hartmann, et al., 2021). The Car-less strains of *Rba. sphaeroides* are unable to
57 assemble an LH2 complex, indicating that Car-BChl interactions are essential to the maintenance
58 of LH2 structural stability (H. P. Lang, Cogdell, Takaichi, & Hunter, 1995). In the LH1 ring of
59 *Rba. sphaeroides*, a combination of two Car groups forms a tightly sealed, impenetrable fence-
60 like structure that blocks the proposed quinone channel of the closed ring (Olsen, Martin, &
61 Hunter, 2017; Qian, Swainsbury, Croll, Salisbury, et al., 2021). However, there are fewer
62 carotenoids in most LH1 structures, so in *Thermochromatium (Tch.) tepidum* and *Rhodospirillum*
63 (*Rsp.*) *rubrum* for example, there are small gaps that allow quinones to cross the ring (Niwa et al.,
64 2014; Qian, Croll, et al., 2021; Yu, Suga, Wang-Otomo, & Shen, 2018b). A point mutation in
65 LH α (W24F) dramatically reduces the amounts of LH1-bound Car. However, in the *pufX*
66 knockout strain of *Rba. sphaeroides*, which possesses a closed LH1 ring composed of 17 LH $\alpha\beta$ s,
67 the same mutation promotes photosynthetic growth (Cao et al., 2022; McGlynn, Hunter, & Jones,
68 1994; Olsen et al., 2017). These observations indicate a correlation between the number of LH1-
69 bound Cars and the architecture and photochemical functions of the RC-LH1. This phenomenon
70 could be further studied using structural information about Car-depleted RC-LH, but no such data
71 have yet been reported.

72 *Roseiflexus castenholzii* is a chlorosome-less filamentous anoxygenic photosynthetic bacterium. It
73 contains only one LH, which forms an unusual RC-LH complex. This complex structurally
74 resembles RC-LH1 but has similar spectroscopic characteristics that are similar to the peripheral
75 LH2 of purple bacteria (Collins et al., 2010; Collins, Xin, & Blankenship, 2009). We previously

76 reported the cryo-electron microscopy (EM) structure of *R. castenholzii* RC-LH at 4.1 Å
77 resolution. It revealed an RC composed of L, M, and cytochrome (cyt) *c* subunits surrounded by
78 an opened elliptical LH ring of 15 LHαβs, with the tetraheme binding domain of cyt *c* protruding
79 on the periplasmic side. The RC is compositionally larger in purple bacteria than in *R.*
80 *castenholzii*, in which it does not contain an H subunit (Pugh, McGlynn, Jones, & Hunter, 1998;
81 Qian, Hunter, & Bullough, 2005; Yamada et al., 2005). However, it does contain a unique cyt *c*
82 transmembrane helix (c-TM) and the newly identified subunit X, both of which flank the gap of
83 the LH ring to form a novel quinone shuttling channel (Xin et al., 2018). Notably, the amino acid
84 sequences of subunit X and TM7, a transmembrane (TM) helix separated from the RC-L and RC-
85 M subunits are unassigned. Pigment analyses have revealed a 2:3 Car : BChl molar ratio of *R.*
86 *castenholzii* RC-LH (Collins et al., 2009). However, the cryo-EM structure resolved only one
87 keto-γ-carotene molecule spanning the interface of each LHαβ, coordinating two B880s and one
88 additional B800 at the periplasmic and the cytoplasmic side, respectively. The lack of a clear
89 cryo-EM density map leaves uncertainty about the presence of additional LH ring-bound Cars, the
90 roles of which are unknown in maintaining the architecture and photochemical functions of the *R.*
91 *castenholzii* RC-LH.

92 We here determined cryo-EM structures of native RC-LH (nRC-LH) complexes purified from *R.*
93 *castenholzii* cells grown under 10,000 lux, 2,000 lux and 100 lux light intensities at 2.8 Å, 3.1 Å
94 and 2.9 Å resolutions, respectively. All three structures shared the same architecture, indicating
95 that the Car composition and assembly are not affected by light intensities. From these high-
96 resolution structures, we identified 14 additional keto-γ-carotene molecules in the exterior of the
97 LH ring (KγC_{ext}). In combination with the B800 on the cytoplasmic side, the newly identified
98 KγC_{ext} molecules blocked the proposed quinone channel between LHαβ subunits, forming a
99 sealed LH ring conformation. We also assigned the full amino acid sequences of subunit X, TM7
100 and an additional TM helix that were derived from hypothetical proteins Y and Z, respectively,

101 and demonstrated their roles in forming the quinone channel and stabilizing the RC-LH
102 interactions. To investigate the role of Cars in the assembly of RC-LH, *R. castenholzii* cells were
103 treated with Car biosynthesis inhibitor diphenylamine (DPA) to produce a Car-depleted RC-LH
104 (dRC-LH); a 3.1 Å-resolution cryo-EM structure of this complex resolved only five keto- γ -
105 carotene molecules bound in the interior of the LH ring ($K\gamma C_{int}$). The absence of subunit X and
106 $K\gamma C_{ext}$ molecules in the dRC-LH produced a LH ring with exposed LH $\alpha\beta$ interface and a larger
107 opening than that of nRC-LH. This conformation accelerated quinone/quinol exchange without
108 affecting the Car-to-BChl energy transfer efficiency. This study thus revealed a previously
109 unrecognized structural basis by which Car assembly regulates the architecture and
110 quinone/quinol exchange rate of the bacterial RC-LH complex. These findings further our
111 understanding of diversity and molecular evolution in the prokaryotic photosynthetic apparatus.

113 Results

114 Identification of $K\gamma C_{ext}$ in the nRC-LH complex

115 To investigate the LH-bound Car numbers and its correlation with the light intensities, we
116 anaerobically cultured *R. castenholzii* cells under the light intensity (2,000 lux) used for obtaining
117 the reported 4.1-Å RC-LH structure (Xin et al., 2018), and also a high and a low light intensity at
118 10,000 lux and 100 lux, respectively. The cell proliferation rate was much faster under 10,000 lux
119 than that grown under 2,000 lux and 100 lux light intensities, and the cells grown under higher
120 light intensities showed a darker reddish-brown color after 120 h of culturing (Figure 1—figure
121 supplement 1A and B). We then isolated and purified nRC-LH complexes from these cells at the
122 stationary growth phase (Figure 1—figure supplement 1C). Ultraviolet (UV)-visible-near infrared
123 (NIR) spectrophotometry of the isolated nRC-LH complexes showed typical Q_y bands at 800 nm
124 (B800) and 880 nm (B880) and a Q_x band at 594 nm, which corresponded to LH-bound BChls.
125 Notably, Car-associated absorption peaks were detected at 457, 482, and 519 nm (Figure 1—

126 [figure supplement 1D](#)). The nRC-LH complexes purified from cells under 10,000 lux, 2,000 lux
127 and 100 lux showed the same Car absorption spectrum ([Figure 1—figure supplement 1E](#)),
128 indicating the pigments content was not affected by light intensities. These nRC-LH complexes
129 were then imaged via cryo-EM, respectively ([Figure 1—figure supplements 2 and 3](#)). Using
130 single particle analysis, the nRC-LH structures obtained from the 10,000 lux, 2,000 lux and 100
131 lux cells were resolved at an overall resolution of 2.8 Å, 3.1 Å and 2.9 Å, respectively ([Figure 1—](#)
132 [figure supplements 2 to 4, Table S2](#)). Superimposition of the 10,000 lux model with that of 2,000
133 lux and 100 lux gave root mean square deviation (RMSD) of 1.753 Å and 1.765 Å, respectively,
134 indicating these three structures share the same architecture.

135 The 15 LH $\alpha\beta$ heterodimers formed an opened elliptical ring surrounding the RC, which contained
136 L, M and cyt *c* subunits; the long and short axes were 112 Å and 103 Å, respectively, and a
137 tetraheme binding domain of cyt *c* protruded into the periplasmic space ([Figure 1A and B](#)).

138 Similar as in most purple bacteria, the RC contained a photo-reactive special pair of BChls, one
139 accessory BChl, three bacteriopheophytins (BPheos), two MQ-11 (MQ_A and MQ_B) and a newly
140 identified MQ_C, and an iron atom to mediate the charge separation and subsequent electron
141 transfer ([Figure 1C](#)). Each LH $\alpha\beta$ non-covalently bound two B880s and one B800 BChl on the
142 periplasmic and cytoplasmic sides ([Figures 1C and 2A](#)). In particular, the LH ring bound 15
143 interior (K γ C_{int}), 14 exterior (K γ C_{ext}) Cars, and an additional K γ C that inserted between the
144 LH $\alpha\beta$ 1 and c-TM in all three structures ([Figure 1B-D, Figure 1—figure supplement 5, Movie S1](#)),
145 indicating both Car compositions and assembly in the nRC-LH were not affected by light
146 intensities. The low-pass filtered cryo-EM map of nRC-LH minus that of the reported 4.1-Å
147 model showed apparent density differences for the K γ C_{ext} ([Figure 1—figure supplement 6A and](#)
148 [B](#)), indicating the K γ C_{ext} molecules were not resolved due to lack of clear EM densities in the 4.1-
149 Å model. Given the similarities between these three nRC-LH structures, we use the 2.8-Å model
150 for following analyses of the nRC-LH structure.

151 **Incorporation of K γ C_{ext} and B800s together blocked the LH $\alpha\beta$ interface**

152 Each LH $\alpha\beta$ heterodimer of *R. castenholzii* was stabilized by hydrogen bonding interactions
153 between LH β -Arg55 and LH α -Asn37 on the periplasmic side, and by LH β -Gln22 and LH α -Arg4
154 on the cytoplasmic side (Figure 2—figure supplement 1A). These interactions were not resolved
155 in the 4.1-Å model, due to lack of clear cryo-EM densities for the Arg4 and Arg55 residues. The
156 LH-bound B880s and one B800 BChl were coordinated by highly conserved His residues on the
157 periplasmic and cytoplasmic sides (Figure 2A, Figure 2—figure supplement 1B). Incorporation of
158 an additional B800 at the cytoplasmic side of the LH ring resembles the exterior L H_h ring of
159 *Gemmatimonas (G.) phototrophica* RC-dLH, in which the B800s were oriented perpendicular to
160 the plane of the membrane (Qian et al., 2022). Superposition of each LH $\alpha\beta$ with that of *G.*
161 *phototrophica* L H_h revealed high overlap at the TM helices, with the exception that the B800
162 porphyrin ring was inclined nearly 60 ° relative to the *G. phototrophica* L H_h -bound B800 (Figure
163 2B). Notably, the B800 conformation was also different from that of B800s bound in *Rba.*
164 *sphaeroides* LH2 and *Rhodopseudomonas (R.) acidophila* LH3, in which the porphyrin rings
165 were both oriented towards the center of the LH ring (Figure 2—figure supplement 1C).
166 Compared to *Tch. tepidum* RC-LH1 that contains a closed LH1 ring, the B800s occupied the
167 space of an N-terminal helix of LH1- α and the head of an ubiquinone (UQ) bound in the LH $\alpha\beta$
168 interface (Figure 2C). Thus, incorporation of the B800s in nRC-LH occupied the LH $\alpha\beta$ interface
169 on the cytoplasmic side.

170 Notably, keto- γ -carotenes in the LH ring of nRC-LH were located at two distinct positions
171 (Figures 1D and 2D). 15 keto- γ -carotene (K γ C_{int}) molecules obliquely spanned the LH $\alpha\beta$
172 subunits, with the 4-oxo- β -ionone rings sandwiched between adjacent LH $\alpha\beta$ s and the ψ -end
173 groups directed into the LH center. In addition, another 14 keto- γ -carotenes were detected in a
174 second position in the LH ring exterior (K γ C_{ext}), which were almost parallel to the adjacent LH β
175 subunits; the 4-oxo- β -ionone rings were directed toward the cytoplasmic side and the ψ -end

176 groups stretched into the periplasm (Figure 2D). Alternatively, a newly identified keto- γ -carotene
177 (K γ C) was sandwiched between LH α β 1 and c-TM, with its 4-oxo- β -ionone ring directing towards
178 the RC-Y subunit (Figure 2E). The B-factor was higher for K γ C_{ext} than for K γ C_{int} molecules, with
179 the latter having lower conformational flexibility (Figure 2—figure supplement 2A).

180 Identification of these Cars yielded in a Car : BChl ratio of approximately 1:1.6 for the nRC-LH
181 structure; this was consistent with results from previous pigment studies (Collins et al., 2009).

182 High performance liquid chromatography (HPLC)-Mass spectrometry (MS) analyses of the
183 pigments in nRC-LH revealed a typical BChl peak at the retention time of 5.58 min, and several
184 peaks of γ -carotene and its derivatives (Figure 2—figure supplement 3). In respect to the
185 complicated Car compositions and lack of specific absorption coefficients of the derivatives, it is
186 impracticable to quantify the Car : Bchl ratio from nRC-LH solution.

187 The nRC-LH thus resembled *Rba. sphaeroides* RC-LH1, which also binds two groups of Cars
188 with different configurations (Tani, Nagashima, et al., 2021). Superposition analyses revealed
189 similar Car positions and orientations between these two structures, although the keto groups of
190 both Car types in nRC-LH were shifted toward the LH α subunits by ~ 6.7 Å (Figure 2—figure
191 supplement 4A and C). Although K γ C_{ext} molecules were not well aligned with the LH α β -bound
192 ubiquinone (UQ) molecule in *Tch. tepidum* RC-LH1, they occupied the space between adjacent
193 LH β s (Figure 2C, Figure 2—figure supplement 4B and D). As a result, the K γ C_{ext} molecules and
194 additional B800s in *R. castenholzii* nRC-LH together blocked the LH α β interface (Figure 2F),
195 which serves as the quinone channel for the closed LH1 ring (Qian et al., 2022; Yu et al., 2018b),
196 and for the opened LH1 ring bound only with interior Cars (Qian, Croll, et al., 2021; Swainsbury
197 et al., 2021; Yu et al., 2018b).

198 **Assignment of the subunit X in nRC-LH complex**

199 The *R. castenholzii* nRC-LH is distinguished from the RC-LH1 of most purple photosynthetic
200 bacteria by a newly identified subunit X and a membrane-bound cyt *c*, which has the TM helices

201 that insert into the gap between LH α β 1 and LH α β 15 to form a putative quinone shuttling channel
202 to the membrane quinone pool (Xin et al., 2018). Unlike the *Rba. sphaeroides* RC-LH1 protein
203 PufX, which interacts with both LH1 and the L and H subunits of the RC (Cao et al., 2022; Tani,
204 Kanno, Kikuchi, et al., 2022), subunit X in *R. castenholzii* was an independent TM helix that did
205 not show any spatial overlap with PufX and PufY from the monomeric *Rba. sphaeroides* RC-LH1
206 (Figure 2—figure supplement 4E). Furthermore, compared with *Tch. tepidum* RC-LH1, which
207 contains a closed LH1 ring, the c-TM of *R. castenholzii* nRC-LH was positioned close to the 16th
208 LH1- α , whereas subunit X showed no overlap with the 16th LH1- β (Figure 2—figure supplement
209 4B). These structural features indicated that *R. castenholzii* RC-LH has evolved different quinone
210 shuttling mechanisms. However, the amino acid sequence of subunit X was unassigned in our
211 previous 4.1-Å model, due to lack of clear cryo-EM densities.

212 From the high-resolution structure of nRC-LH, we successfully assigned the amino acid sequence
213 (Met1-Ser26) for subunit X, which was derived from a hypothetical protein containing 32 amino
214 acid residues (Figure 2G and H). This polypeptide was encoded by coding sequences (CDS:
215 1,060,366-1,060,464) in *R. castenholzii* (strain DSM 13941/HLO8) genome, but it was not
216 annotated in the Protein Database of Uniprot and NCBI. The amino acid sequence of subunit X
217 showed strict conservation with a hypothetical protein KatS3mg058_1126 (GenBank:
218 GIV99722.1) from *Roseiflexus sp.*, which was denoted by metagenomic analyses of the
219 uncultivated bacteria in Katase hot spring sediment (Kato, Masuda, Shibata, Shirasu, & Ohkuma,
220 2022) (Figure 2—figure supplement 5). The resolved subunit X inserted into the LH opening in
221 opposite orientation with that of LH α β and c-TM, where these TM helices were stabilized by
222 hydrophobic and weak hydrogen bonding interactions (Figure 2G and I). On the cytoplasmic side,
223 the C-terminus of subunit X was coordinated in a pocket formed by the cyt *c* N-terminal region
224 (Leu8, Phe9 and Thr13), LH β 15 (Val25 and Ile28), and the 4-oxo- β -ionone ring of a K γ C_{int}
225 molecule. A weak hydrogen bond (3.5 Å) formed between the Met25 main chain nitrogen of

226 subunit X and Arg19 amino nitrogen of c-TM. These pigment-protein interactions together
227 stabilized the conformation of subunit X (Figure 2I, Movie S2).

228 **Stabilizing the RC-LH interactions by newly assigned proteins Y and Z**

229 Superposition of the RC structure with that of purple bacteria showed excellent matches at the L
230 and M subunits, each of which contained five TM helices. Unlike purple bacteria, *R. castenholzii*
231 L and M subunits are encoded by a fused gene *pufLM* but processed into two independent
232 peptides in the complex (Collins et al., 2010; Collins et al., 2009; Yamada et al., 2005). In current
233 model, RC-L subunit contains TM1-5 and terminates at Ala315, whereas the TM6-10 composed
234 RC-M starts from Pro335 (Figure 3A, Figure 3—figure supplement 1A and C). In addition, *R.*
235 *castenholzii* RC-L contains an N-terminal extension (Met1-Pro35) that was solvent exposed on
236 the cytoplasmic side (Figure 3B, Figure 3—figure supplement 1A and C). Most importantly, we
237 resolved two additional TM helices in the RC (Figure 3A). Near the TM5 from RC-L and c-TM, a
238 separate TM helix (corresponding to the TM7 in previous 4.1-Å model) was resolved with amino
239 acid residues (Met1-Pro32) from a hypothetical protein Y (Figure 3C). Similar as subunit X, this
240 protein was encoded by CDS (1,089,486-1,089,602) from *R. castenholzii* (strain DSM
241 13941/HLO8) genomic DNA, but it was not annotated in Protein Database as well. Coincidentally,
242 the amino acid sequence of protein Y was conserved with a hypothetical protein
243 KatS3mg058_1154 (GenBank: GIV99750.1) from *Roseiflexus sp* (Figure 2—figure supplement
244 5). The N-terminal region of protein Y was inclined towards the c-TM on the periplasmic side,
245 wherein the 4-oxo- β -ionone ring of K γ C was coordinated by hydrogen bonding interactions with
246 Met11 (3.4 Å) from Y, Ser35 (3.0 Å) and Trp40 (2.8 Å) from the c-TM. On the cytoplasmic side,
247 protein Y was stabilized by hydrogen bonding interactions with the TM5 of RC-L (Figure 3B).
248 Unlike purple bacteria, *R. castenholzii* RC does not contain an H subunit. Instead, we identified
249 an individual TM helix between the LH α 11 and RC-M (Figures 1B and 3D-E). Superposition
250 revealed mismatch of this TM helix with that of the purple bacterial H subunit (Figure 3A). This

251 helix was assigned to cover the amino acid residues Ser12 to Asn58 of a hypothetical protein
252 (WP_041331144.1) from *R. castenholzii* (strain DSM 13941/HLO8) (Figure 3D), we named it
253 protein Z. This protein was verified with a sequence coverage of 19 % by peptide mass
254 fingerprinting (PMF) analyses of the Blue-Native PAGE of nRC-LH (Table S1). The resolved
255 protein Z was stabilized by hydrogen bonding and hydrophobic interactions with amino acid
256 residues from the RC-M and LH α 11 on the periplasmic and cytoplasmic sides (Figure 3E).
257 In contrast with most purple bacteria, *R. castenholzii* cyt *c* contains an N-terminal transmembrane
258 helix c-TM, which was absent in *G. phototrophica* and *Tch. tepidum* RC-bound cyt *c*, and was
259 even distinct from *Rhodospila (Rpi.) globiformis* cyt *c* that also contains an N-terminal TM helix
260 (Tani, Kanno, Kurosawa, et al., 2022) (Figure 3F, Figure 3—figure supplement 1B and C).
261 Compared to *Rpi. globiformis* cyt *c*, the c-TM was obliquely inserting into the LH opening in an
262 opposite direction, wherein it formed a potential quinone shuttling channel with the subunit X
263 (Figure 3F). The N-terminal cytoplasmic region of c-TM was stabilized by extensive hydrophobic
264 interactions with LH α β 15 and LH α β 1 (Figure 2I). These included interactions between the cyt *c*
265 Ile27, Phe20, and Val16 sidechains and the LH β 1 Trp14, Leu17 and Pro16 sidechains. The main
266 chain oxygen of Leu8 formed a hydrogen bond with the guanidine nitrogen of Arg9 from LH α 15
267 (3.2 Å). Notably, cyt *c* also formed extensive hydrogen bonding interactions with the RC-L and
268 RC-M subunits at the heme3-binding region (Figure 3—figure supplement 2A). In addition to the
269 protein Y, Z and cyt *c* mediated interactions, another two close contact points were evident
270 between the RC and LH; (i) helix 1 (TM1) from RC-L to LH α 13, (ii) TM6 from RC-M to LH α 4
271 and LH α 5 (Figure 3—figure supplement 2B). We also identified several structured lipids
272 (phosphatidylglycerol, PG; and diglyceride, DG) within the interface between the RC and LH
273 subunits (Figure 3G and H), these protein-lipids contacts further stabilized the nRC-LH complex.
274 **Car-depleted RC-LH (dRC-LH) lacked subunit X**

275 To explore the structural and functional relationships between LH-bound Cars and the RC-LH
276 complex, *R. castenholzii* cells were photoheterotrophically cultured in the presence of DPA, a Car
277 biosynthesis inhibitor for photosynthetic bacteria (Gall, Henry, Takaichi, Robert, & Cogdell,
278 2005). In response to DPA-treatment, bacterial growth curves clearly indicated a decreased
279 proliferation rate of cells grown under 10,000 lux, confirming the important roles of Cars in
280 photosynthesis and cell proliferation (Figure 1—figure supplement 1A and B). Interestingly, DPA
281 treatment did not affect the growth of cells illuminated under 2,000 lux and 100 lux, which
282 showed an overall much lower proliferation rate (Figure 1—figure supplement 1B).

283 Concomitantly, the color of the growing cells changed progressively from brownish red in the
284 first culture to light yellow in the fifth sub-culture (Figure 1—figure supplement 1A), indicating
285 gradual inhibition of Car biosynthesis during sub-culturing. To confirm the effects of DPA
286 treatment on Car incorporation into the RC-LH, dRC-LH complexes were isolated from each
287 successive sub-culture of DPA-treated *R. castenholzii* cells (Figure 1—figure supplement 1F).

288 There was a striking decrease in Car absorbance in dRC-LH complexes extracted from the third
289 through fifth sub-cultures of DPA-treated cells compared to nRC-LH extracted from untreated
290 cells (Figure 1—figure supplement 1D and E). Additionally, HPLC analysis of dRC-LH isolated
291 from the fifth sub-culture of DPA-treated cells showed same pigment compositions but decreased
292 absorbance compared to the nRC-LH (Figure 2—figure supplement 3B).

293 To illustrate the effects of DPA treatment on the RC-LH architecture, we determined the cryo-EM
294 structure of dRC-LH isolated from the fifth sub-culture of DPA-treated *R. castenholzii* cells at 3.1
295 Å resolution (Figure 4A and B, Figure 4—figure supplement 1). The most obvious difference
296 between these two structures was the absence of the entire X subunit and the cytoplasmic region
297 of cyt *c* subunit (Pro6-Val16) in the dRC-LH; both were located at the LH opening of nRC-LH
298 (Figure 4C, Movie S2). Notably, only five K γ C_{int} molecules were resolved (which spanned the
299 LH α β 5, 7, 9, 10 and 11 heterodimers in the dRC-LH structure), whereas none of the K γ C_{ext}

300 molecules were observed (Figure 4B, Figure 1—figure supplement 4C, Movie S1). The five
301 existing $K\gamma C_{int}$ molecules were located relatively far from the LH opening (~ 52 Å), which is
302 where Cars with the highest B-factors were distributed, indicating an unstable conformation
303 (Figure 2—figure supplement 2A). Additionally, the five $K\gamma C_{int}$ molecules in dRC-LH adopted
304 the same conformation and a similar edge-to-edge distance from LH-bound B800/B880s as the
305 corresponding $K\gamma C_{int}$ molecules did in nRC-LH (Figure 4D, Tables S3 and S4). The absence of
306 $K\gamma C_{ext}$ and most $K\gamma C_{int}$ molecules in the LH ring confirmed that DPA treatment decreased the
307 numbers of LH-bound Cars in the dRC-LH.

308 The dimensions of the LH ring in dRC-LH increased by ~ 3.0 Å at the major axes and by ~ 2.0 Å
309 at the minor axes, although both the protein subunits and cofactors in the RC adopted the same
310 conformations as they did in nRC-LH (Figure 5—figure supplement 1A). Moreover, the distances
311 between adjacent LH α s and LH β s in the dRC-LH showed average increases of 0.5 Å and 1.0 Å,
312 respectively, compared with nRC-LH (Table S5). Accordingly, the Mg-to-Mg distances between
313 adjacent B880s and B800s also increased in dRC-LH (Tables S6 and S7). Specifically, the LH-
314 bound B880s and B800s shifted away from the LH ring center by ~ 2.0 Å, consequently increasing
315 the Mg-to-Mg distance between LH-bound B880s and the nearest special pair of BChls in the RC
316 (Figure 4E, Table S8). These results therefore indicated that Car depletion not only decreased the
317 number of LH-bound Cars, but also altered the conformation of dRC-LH. These alterations could
318 affect the efficiency of energy transfer during the primary photochemical reactions (Sener et al.,
319 2011; Xin, Pan, Collins, Lin, & Blankenship, 2012).

320 **Conformational changes in the dRC-LH accelerated quinone/quinol exchange**

321 In nRC-LH, insertion of the c-TM and subunit X at the LH opening, wherein the N-terminal
322 cytoplasmic region of c-TM was stabilized by extensive hydrophobic and weak hydrogen bonding
323 interactions with subunit X, LH $\alpha\beta 15$ and LH $\alpha\beta 1$ (Figures 2I and 4C). The c-TM was closer to
324 LH $\alpha 1$ (9.7 Å) than to LH $\alpha 15$, whereas subunit X was closer to LH $\beta 15$ (11.2 Å), creating a narrow

325 gap between the c-TM and the LH $\alpha\beta$ 15 (Figure 4C and F, Table S5). The B800 pigment was not
326 detected between c-TM and LH α 15 (Figure 4C). Thus, the c-TM and subunit X were positioned
327 to the sides of LH α 1 and LH β 15, respectively; this formed a 19.4-Å gap between the c-TM and
328 LH α 15, and a 28-Å gap between subunit X and LH β 1, both of which may have allowed reduced
329 quinones to exit the LH to the membrane quinone pool. Because dRC-LH lacked subunit X, the
330 gap between LH β 1 and LH β 15 increased to ~38.0 Å (Figure 4C and F).

331 To investigate the functional effects of this conformational change, we compared the
332 quinone/quinol exchange rates for nRC-LH and dRC-LH complexes. In the cyclic electron
333 transport chain of *R. castenholzii*, the periplasmic electron acceptor auracyanin (Ac) transfers
334 electrons back to the RC special pair through the tetra-heme of cyt *c* subunit, reducing the photo-
335 oxidized special pair for turnover of the photo-reaction and electron transfer that subsequently
336 reduce the bound menaquinones (MQ_A and MQ_B) in the RC. The reduced MQH₂ is released from
337 its binding site and exchanges with free MQs outside the RC-LH (Figure 4G). Using sodium
338 dithionite-reduced Ac as the electron donor and menaquinone-4 as the electron acceptor, we
339 measured Ac absorbance changes at 604 nm with varied concentrations of menaquinone-4 (Figure
340 5—figure supplement 1B and C). The initial oxidation rate of Ac was markedly higher in the
341 presence of dRC-LH than nRC-LH (Figure 4H). This was consistent with the determined apparent
342 Michaelis constants, which showed that dRC-LH had an accelerated quinone/quinol exchange
343 rate of 6.12 ± 0.62 μM min⁻¹ (Table S9). The accelerated quinone/quinol exchange rate in dRC-LH
344 was probably resulted from exposure of the LH $\alpha\beta$ interface by Cars depletion, and also the
345 increased gap dimension of the LH ring.

346 **Carotenoid depletion did not affect the Car-to-BChl energy transfer efficiency**

347 To elucidate the effects of Cars depletion on the Car-to-BChl energy transfer efficiency of the
348 RC-LH, we firstly examined the configurations and coordinating environments of the LH-bound
349 Cars. K γ C_{int} molecules spanned the TM region of each LH $\alpha\beta$ heterodimer; the heads were

350 inserted into the hydrophobic pocket formed by the LH α and LH β subunits, the phytol tails of two
351 B880s, and the B800 porphyrin ring. On the periplasmic side, the ψ -end group of K γ C_{int} was
352 directed into a hydrophobic patch formed by two adjacent LH α subunits (Figure 5A left).
353 Alternatively, the newly-identified K γ C_{ext} molecules were immobilized in a position that was
354 nearly parallel to the adjacent LH β s. The heads were inserted into a cavity formed by the B800
355 porphyrin ring and two adjacent LH β s, and their tails extended along the adjacent LH β s,
356 stabilized by hydrophobic interactions (Figure 5A right). However, depletion of these K γ C_{ext}
357 molecules in dRC-LH prevented the tight packing of the K γ C_{int} molecules with LH $\alpha\beta$
358 heterodimers. Thus, in the absence of K γ C_{ext}, the head of each K γ C_{int} molecule shifted towards
359 the B800 porphyrin ring, which moved the head out from the center of the LH ring by ~ 3.0 Å
360 (Figure 5B). However, the edge-to-edge distances of K γ C_{int} to the B800/B880s remained similar
361 between dRC-LH and nRC-LH (Table S3).

362 We next measured the fluorescence excitation and absorption spectra of the nRC-LH and dRC-
363 LH complexes to calculate the Car-to-BChl energy transfer efficiency. Most RC-LH fluorescence
364 is emitted from the B880 Qy band (Collins et al., 2009). Excitation of nRC-LH at 470 nm yielded
365 emissions at 900 nm, whereas dRC-LH excitation produced emissions at 905 nm (Figure 5C).
366 This shift of the emission peak indicated changes in the LH ring pigment configuration between
367 the two complexes. The intensity ratio of fluorescence excitation spectra to absorption spectra,
368 expressed as the 1-T of RC-LH, was then calculated. The results revealed that the Car-to-BChl
369 energy transfer efficiency remained similar between nRC-LH (44%) and dRC-LH (46%) (Figure
370 5D). Car-to-BChl energy transfer in the LH is closely related to the number of Car conjugated
371 double bonds, the relative distances between Cars and BChls, and Car/BChl spatial organization
372 (Polivka & Frank, 2010). In *R. castenholzii*, each keto- γ -carotene contains 11 conjugated double
373 bonds (Collins et al., 2009). Although all K γ C_{ext} and most K γ C_{int} molecules were depleted in
374 dRC-LH, the five remaining K γ C_{int} molecules adopted the same configuration and similar edge-

375 to-edge distances with LH-bound B800/B880s as that in the nRC-LH (Figure 4D, Table S3).
376 Therefore, Car depletion from the LH ring in dRC-LH did not affect interactions between the
377 remaining Cars and BChls, which exhibited similar excitation energy transfer values in dRC-LH
378 and nRC-LH complexes. These results suggested that the existing Car-to-BChl energy transfer
379 efficiency is similar even though there is variation in the number of LH-bound Cars.

380

381 Discussion

382 Unlike the well-studied purple photosynthetic bacteria, which contain two types of LH
383 complexes, *R. castenholzii* contains only one RC-LH complex for light harvesting and primary
384 photochemical reactions. It does not contain the H subunit that is typically found in purple
385 bacteria (Pugh et al., 1998; Qian et al., 2005; Yamada et al., 2005). Especially, *R. castenholzii*
386 RC-LH contains a tetra-heme cyt *c* subunit that interrupts the LH ring, which is composed of 15
387 $\alpha\beta$ -polypeptides, through a novel N-terminal TM helix; together with the newly identified subunit
388 X, this forms a potential quinone shuttling channel on the LH ring. In the present study, we
389 determined high resolution cryo-EM structures of nRC-LH, from which we assigned the full
390 amino acid sequence of subunit X, and two additional TM helices derived from hypothetical
391 proteins Y and Z in the RC, which both functioned in stabilizing the RC-LH interactions. Most
392 importantly, we identified 14 additional keto- γ -carotene molecules ($K\gamma C_{ext}$) in the LH ring
393 exterior, and one $K\gamma C$ inserted between $LH\alpha\beta 1$ and *c*-TM, which generated a 2:3 Car : BChl
394 molar ratio consistent with previous pigments analyses (Collins et al., 2009). Binding of the
395 internal and external keto- γ -carotenes together with the B800s blocked the proposed quinone
396 channel between $LH\alpha\beta$ subunits. DPA treatment of the cells yielded a Car-depleted RC-LH,
397 referred to as dRC-LH; a 3.1-Å resolution cryo-EM structure resolved only five $K\gamma C_{int}$ molecules,
398 and the absence of subunit X and the cytoplasmic region of *c*-TM. These alterations in the dRC-

399 LH increased the size of the LH opening and exposed the LH $\alpha\beta$ interface, accelerating the
400 quinone/quinol exchange rate, without affecting the Car-to-BChl energy transfer efficiency.
401 To maintain continuous photo-reaction and turnover of the electron transport chain, two quinone
402 exchange/transport routes are required for the bacterial RC-LH1 complex. One is the exchange
403 route for the free/bound quinone in the RC, which was represented by a newly identified MQc in
404 our nRC-LH structure (Figure 3H), and also extra ubiquinone molecules found in many purple
405 bacterial RCs (Cao et al., 2022; Kishi et al., 2021; Qian et al., 2022; Qian, Siebert, Wang,
406 Canniffe, & Hunter, 2018; Swainsbury et al., 2021; Tani, Kanno, Kurosawa, et al., 2022; Yu,
407 Suga, Wang-Otomo, & Shen, 2018a). The other one is shuttling channel between the inside and
408 outside of the LH1 ring. For *Tch. tepidum* RC-LH1 that contains an almost symmetric and
409 completely closed LH1 ring, except the ‘waiting’ UQ8 identified near Q_B, one UQ8 was found to
410 be inserted between the LH1 α and LH1 β subunits (Yu et al., 2018a), representing a potential
411 quinone exchange channel between the LH $\alpha\beta$ interface. Therefore, the space between the LH $\alpha\beta$
412 subunits can serve as quinone exchange channel for the closed LH1 ring (Qian et al., 2022; Yu et
413 al., 2018b), and also for the opened LH1 ring bound only with interior Cars (Qian, Croll, et al.,
414 2021; Swainsbury et al., 2021; Yu et al., 2018b). For most purple bacterial RC-LH1 complexes
415 with an opened C-shaped LH1 ring, reduced quinones are also shuttled from the RC through a gap
416 at the LH1 ring, which is disrupted by protein W, or PufX and PufY (or protein -U) (Cao et al.,
417 2022; Jackson et al., 2018; Qian, Croll, et al., 2021; Tani, Kanno, et al., 2021; Tani, Kanno,
418 Kikuchi, et al., 2022; Tani, Nagashima, et al., 2021).

419 Distinct from the RC-LH1 of most purple bacteria, each LH $\alpha\beta$ of *R. castenholzii* non-covalently
420 bound an additional B800 BChl at the cytoplasmic side, which occupied the LH $\alpha\beta$ interface at the
421 cytoplasmic side (Figure 2C, Figure 2—figure supplement 1C). In addition, we identified keto- γ -
422 carotenes at three distinct positions in the nRC-LH ring: internal (K γ C_{int}) and external (K γ C_{ext}),
423 and also an additional K γ C near the LH opening (Figures 1D and 3B). The K γ C_{int} molecules

424 embedded between the LH $\alpha\beta$ s had a similar conformation as they do in the completely closed and
425 also the opened LH1 ring of purple bacteria. In contrast, K γ C_{ext} molecules occupied the space
426 between adjacent LH β s, although they were not well aligned with the *Tch. tepidum* LH $\alpha\beta$ bound
427 UQ8 molecule (Figure 2C, Figure 2—figure supplement 4D). Therefore, incorporation of the
428 K γ C_{ext} molecules and additional B800s in *R. castenholzii* nRC-LH together blocked the LH $\alpha\beta$
429 interface for quinone exchange (Figure 2F). Alternatively, *R. castenholzii* RC-LH incorporated a
430 membrane-bound cyt *c* and a hypothetical protein X, which has the TM helices that interrupted
431 the LH ring to form a narrow channel for controlled quinone/quinol exchange (Figure 6).
432 Superposition of *R. castenholzii* with purple bacterial RC-LH1s revealed distinct locations and
433 orientations of subunit X and c-TM compared to PufX and PufY (Figure 2—figure supplement
434 4E), indicating *R. castenholzii* has evolved different quinone shuttling mechanisms.
435 Genetic depletion of the LH1-bound Cars promoted the photosynthetic growth of a PufX-
436 knockout *Rba. sphaeroides* mutant with a closed LH1 ring (Cao et al., 2022; McGlynn et al.,
437 1994; Olsen et al., 2017); this implies that disruption of Cars binding exposed the blocked
438 quinone channel between LH $\alpha\beta$ interface and facilitated the quinone exchange, thus promoting
439 photosynthetic growth. In our study, depletion of the K γ C_{ext} and most K γ C_{int} molecules by DPA
440 treatment could also expose the space between LH $\alpha\beta$ subunits. In addition, absence of the subunit
441 X and cytoplasmic region of c-TM in dRC-LH broadened the dimensions of the LH ring opening,
442 which together accelerated the quinone/quinol exchange rate of the dRC-LH (Figure 6). This was
443 consistent with a previous observation that the open form of the *Rhodospseudomonas (Rps.)*
444 *palustris* RC-LH1 has a faster quinone diffusion rate than the closed form (Swainsbury et al.,
445 2021). Notably, depletion of most LH-bound Cars only affected the stable conformation of the
446 cytoplasmic region of c-TM, which was closely associated with subunit X to form the quinone
447 channel (Figure 2I). Compared to cyt *c* subunit that formed extensive hydrogen bonding
448 interactions with the L, M and Y of the RC, the subunit X was characterized by high B-factors,

449 fewer contacts with the RC-LH, and an easily disrupted conformation (Figures 3B and 4C, Figure
450 2—figure supplement 2B). Especially, the subunit X was derived from a hypothetical protein that
451 inserted into the LH opening in an opposite orientation with LH $\alpha\beta$ and c-TM, suggesting that it
452 was likely the last subunit incorporated into the RC-LH. Therefore, *R. castenholzii* RC-LH could
453 evolve the subunit X to control the conformation of the quinone shuttling channel.

454 Cars contribute to the self-assembly of natural α/β polypeptides to form LH1 complexes in vitro
455 (Fiedor, Akahane, & Koyama, 2004), Car-less *Rhodospirillum rubrum* LH1 can be obtained by
456 exogenous recombination (Parkes-Loach, Sprinkle, & Loach, 1988). In the carotenoid-less *Rba.*
457 *sphaeroides* mutant strain R26, the polymerized form of RC-LH is predominantly monomeric,
458 and the curvature of the photosynthetic membrane is altered due to the lack of dimeric RC-LH
459 (Ng et al., 2011). This implies that Cars assembly can regulate the conformation of the RC-LH
460 complex. In our study, although the extensive interactions between subunit X, c-TM and LH $\alpha\beta$ 15
461 & LH $\alpha\beta$ 1 were disrupted in dRC-LH (Figures 2I and 4C), the correlation between Car depletion
462 and the absence of subunit X has not been adequately verified. Since DPA treatment is not a clean
463 way to examine the effect of Cars, it left several interior Cars still bound to the LH ring. DPA is a
464 broad-spectrum inhibitor that slows cellular metabolic processes and specifically affects Car
465 biosynthesis by inhibiting phytoene desaturase (CrtI), an essential enzyme catalyzes conversion of
466 the colorless Car precursor phytoene to the colored lycopene (Bramley, 1993). We here found that
467 DPA treatment not only dramatically decreased the *R. castenholzii* proliferation rate but also
468 depleted the LH-bound Cars in dRC-LH (Figures 1A and 4, Figure 1—figure supplement 1B).

469 Although DPA treatment did not strikingly affect cell proliferation grown under 2,000 lux and
470 100 lux light intensities, it still decreased the Car absorbance of the extracted dRC-LH (Figure
471 1—figure supplement 1E). Therefore, an efficient genetic manipulation system of *R. castenholzii*
472 is required for elucidating the correlations between Cars and the RC-LH assembly, as well as the
473 photosynthetic growth of cells.

474 In summary, this study revealed conformational changes of the *R. castenholzii* RC-LH in the
475 presence and absence of K γ C_{ext} and subunit X, which played an important role in regulating the
476 conformation and quinone/quinol exchange rates. K γ C_{ext} incorporation results in a sealed
477 conformation of the LH ring, whereas Car depletion and absence of the subunit X produces an
478 exposed LH ring with larger opening, which together accelerate the quinone/quinol exchange rate.
479 These results demonstrate a correlation between LH-bound Cars and the assembly and
480 quinone/quinol exchange of *R. castenholzii* RC-LH. Overall, these findings deepen our
481 understanding of the light absorption and photo-reaction mechanisms in prokaryotic
482 photosynthesis and increase the feasibility of applying prokaryotic photosystems in synthetic
483 microbiology approaches.

484

485

486 **Materials and methods**

487 **Extraction and purification of the RC-LH complexes from *Roseiflexus castenholzii***

488 The *Roseiflexus castenholzii* cells (strain HLO8^T) were grown anaerobically at 50 °C under
489 10,000 lux, 2,000 lux and 100 lux light intensities in a modified PE medium as previously
490 reported (Hanada, Takaichi, Matsuura, & Nakamura, 2002). To inhibit carotenoid biosynthesis,
491 diphenylamine (DPA) was added to the medium (12 mg L⁻¹), and the bacteria were cultured under
492 the same conditions as the native bacteria. Growth curves of the native and DPA-treated *R.*
493 *castenholzii* cells were monitored with a UV-vis spectrophotometer (Mapada P6, Shanghai), by
494 recording the absorption of cultured cells at 660 nm for every 12 hours. The mean values of the
495 optical density at each time point and the standard deviations of mean (n=3) were calculated.
496 Isolation and purification of both the nRC-LH and dRC-LH complexes were carried out as
497 described (Collins et al., 2009) with some modifications. The whole membranes (OD=20 cm⁻¹
498 measured at 880 nm) in 20 mM Tris-HCl (pH 8.0) were solubilized by 0.45 % (w/v) β -DDM at

499 room temperature for 1 hour with gentle stirring and then were ultra-centrifuged at 200,000 $\times g$ for
500 1 hour. The supernatant was collected and filtered through a 0.22 μm filter and diluted with buffer
501 A (0.04 % DDM, 50 mM Tris-HCl, pH 8.0), subsequently loaded on an anion exchange
502 chromatography column (HiTrap Q HP, Cytiva, USA) that had been equilibrated with buffer A.
503 The crude RC-LH complex was eluted from the column with 200 mM NaCl in buffer A, and
504 further purified by gel filtration through a Superdex 200 16/600 column, and a Superose 6
505 Increase 10/300 GL (Cytiva, USA) in buffer B (0.04 % DDM, 100 mM NaCl, 50 mM Tris-HCl,
506 pH 8.0). The whole preparation procedure was monitored by detecting the absorption spectrum
507 from 250 to 900 nm.

508 **HPLC-MS analyses of the pigments in RC-LH complexes**

509 Pigment composition was analyzed by High performance liquid chromatography (HPLC) as
510 described (Collins et al., 2009) The RC-LH samples were mixed with acetone / methanol (v / v
511 ratio of 7:2) to extract the pigments, followed by centrifugation at 12,000 $\times g$ for 15 min. Then the
512 supernatant was filtered through a 0.22 μm filter membrane. The filtrate was injected into a C18
513 reversed-phase column (4.6 mm \times 150 mm, 5 μm particle size, Agilent, USA) in a Thermo-Fisher
514 Ultimate 3000 separation module equipped with a DAD-3000 Diode Array Detector. The
515 pigments were eluted at a flow rate of 1 mL min⁻¹ using 100% methanol. Pigments were then
516 detected by their absorbance at 442 nm and 772 nm. The commercial BChl *a* and γ -carotene
517 (Sigma-Aldrich) were used as standards. Pigments were identified based on their absorption
518 spectra, retention times and further analyzed by LC-MS. LC-MS was equipped with an Agilent
519 1200 HPLC system (Agilent, Santa Clara, CA, USA) and a Thermo Finnigan LCQDeca XP Max
520 LC/MS system (Thermo Finnigan, Waltham, MA, USA). The condition of HPLC is the same as
521 the above. MS with an atmospheric pressure chemical ionization (APCI) source was performed as
522 follows: positive mode, source voltage of 2.5 kV, capillary voltage of 46 V, sheath gas flow of 60

523 arbitrary units, auxiliary/sweep gas flow of 10 arbitrary units, capillary temperature 150 °C. The
524 pigments composition was determined as shown in Figure S9.

525 **Cryo-electron microscopy**

526 Three μL aliquots of the purified RC-LH (native and carotenoid depleted) complexes were placed
527 on glow-discharged CryoMatrix R1.2/1.3 300-mesh amorphous alloy film (product no. M024-
528 Au300-R12/13, Zhenjiang Lehua Technology Co. Ltd., China). Each grid was blotted for 3 s at
529 4 °C in 100 % humidity, then plunged into liquid ethane with a Mark IV Vitrobot system (Thermo
530 Fisher Scientific, USA).

531 Data for the native RC-LH (nRC-LH) complex was collected on a 300 kV Titan Krios electron
532 microscope (Thermo Fisher Scientific, USA) with a K3 direct electron detector (Gatan, USA) in
533 counting mode. A total of 2,836 movies were recorded at a magnification of $\times 64,000$ and a pixel
534 size of 1.08 Å, with a total dose of approximately $50 \text{ e}^- \text{ \AA}^{-2}$, and a defocus range between -1.0 and
535 -2.3 μm . Each movie was collected over 2.59 s and dose-fractionated into 40 frames. Data for the
536 carotenoid depleted RC-LH (dRC-LH) complex was recorded on a 300 kV Titan Krios electron
537 microscope with a K3 direct electron detector in counting mode. A nominal magnification of
538 $81,000 \times$ was used for imaging, which yielded a pixel size of 0.893 Å. A total of 3,514 movies
539 were collected with defocus values between -1.1 and -1.7 μm . Each movie was dose-fractionated
540 to 40 frames under a total dose rate of $49.65 \text{ e}^- \text{ \AA}^{-2}$ and an exposure time of 2.2 s. Cryo-EM
541 analyses of nRC-LH complexes extracted from cells grown under 2,000 lux and 100 lux were
542 summarized in figure supplement3 and table S2.

543 **Image processing**

544 Beam-induced motion correction and exposure weighting were performed by MotionCorr2
545 (Zheng et al., 2017), and the CTF (contrast transfer function) was estimated using the Gctf
546 program (Zhang, 2016). The automatic particle picking was performed by Gautomatch

547 (developed by K. Zhang, <https://www.mrc-lmb.cam.ac.uk/kzhang/Gautomatch/>) and RELION.
548 All other steps were performed using RELION 3.1 (Zivanov et al., 2018).
549 For the dataset of native RC-LH (nRC-LH) complex extracted from cells grown under 10,000 lux,
550 the templates for automatic particle picking were 2D class averages of manually picked 3,106
551 particles. In total, 1,625,156 particles were auto-picked from 2,836 micrographs. The picked
552 particles were extracted at 4×4 binning and subjected to two rounds of 2D classification. Good
553 2D class averages in different orientations were selected to generate the initial model. A subset of
554 1,041,360 particles at the original pixel size were selected for 3D classification into three classes
555 with the initial model as a reference, and then 372,029 good particles were refined into a 3.7-Å
556 resolution electron density map. Finally, the resultant data refined by per-particle CTF refinement
557 were subjected to 3D refinement and postprocessing to 2.8 Å resolution on the gold-standard FSC
558 (Fourier Shell Correlation) = 0.143 criterion. The image processing of nRC-LH complexes
559 extracted from cells grown under 2,000 lux and 100 lux were summarized in figure supplement3.
560 For the dataset of carotenoid depleted RC-LH (dRC-LH) complex, a total of 1,081,719 particles
561 were automatically picked from 3,514 micrographs. The picked particles were extracted at 4×4
562 binning and subjected to three rounds of reference-free 2D classification, resulting in 191,821
563 particles being left and re-extracted into the original pixel size of 0.893 Å. After 3D classification
564 with three classes of particles, a subset of 84,352 particles was selected for the final refinement
565 and postprocessing. The resolution of the final map was 3.5 Å. The values of the angular
566 distribution of particles from 3D refinement were visualized by ChimeraX (Pettersen et al., 2021).
567 Local resolution was estimated with Resmap (Kucukelbir, Sigworth, & Tagare, 2014).

568 **Model building and refinement**

569 The reported 4.1-Å resolution model of RC-LH complex from *Roseiflexus castenholzii* (PDB ID:
570 5YQ7) (Xin et al., 2018) was fitted into the density map in ChimeraX. Based on the density map,
571 the structural model of the native RC-LH (nRC-LH) complex, including the amino acids residues,

572 cofactors, lipids and the newly identified exterior keto- γ -carotene ($K\gamma C_{\text{ext}}$ and $K\gamma C$) molecules
573 were manually built and adjusted in Coot (Emsley & Cowtan, 2004). Then real-space refinement
574 in PHENIX (Adams et al., 2010) was used for model refinement with intra-cofactor and protein-
575 cofactor geometric constraints. The structure of the carotenoid depleted RC-LH (dRC-LH)
576 complex was also manually built using the refined model of nRC-LH as a reference in COOT
577 (Emsley & Cowtan, 2004) and refined using the real-space refinement in PHENIX (Adams et al.,
578 2010). The refinement and model statistics are listed in table S2.

579 **Assignment of the subunit X, proteins Y and Z**

580 The Cryo-EM Map of nRC-LH was used for automated model building in ModelAngelo, a
581 program developed by Professor Sjors Scheres (<https://arxiv.org/abs/2210.00006v1>). BLAST
582 search of the deduced amino acid sequences of subunit X generated a hint with hypothetical
583 protein KatS3mg058_1126 (GenBank: GIV99722.1) from *Roseiflexus sp*, which was denoted by
584 metagenomic analyses of the uncultivated bacteria in Katase hot spring sediment (Kato et al.,
585 2022). However, this polypeptide has not been annotated in the Protein Database of *R.*
586 *castenholzii* (strain DSM 13941/HLO8). By searching the genomic DNA of *R. castenholzii* (strain
587 DSM 13941/HLO8), we eventually identified the coding sequences (CDS: 1,060,366-1,060,464)
588 of subunit X, which shared strictly conserved amino acid sequence with KatS3mg058_1126. The
589 assigned amino acid residues fitted well with the cryo-EM densities as shown in Figure 2H.
590 Assignment of protein Y and Z was performed in same procedure, except that protein Z was also
591 confirmed by PMF analyses shown in table S1.

592 **Steady-state and fluorescence spectroscopy**

593 Absorption spectra of the RC-LH complexes were collected at wavelength ranging from 250 to
594 900 nm using a UV-vis spectrophotometer (Mapada P6, Shanghai). Fluorescence emission and
595 excitation spectra of the nRC-LH and dRC-LH complexes were recorded using a steady-state and
596 time-resolved Photoluminescence Spectrometer (Edinburgh FLS1000, UK), equipped with a

597 Hamamatsu NIR PMT detector (Hamamatsu Photonics, Japan) and an external adjustable 980 nm
598 continuous-wave (CW) laser. The fluorescence excitation spectra were obtained with emissions
599 monitored at 920 nm, and excitation at 470 nm was used for emission spectra.

600 **Auracyanin oxidation assays**

601 Isolation and purification of endogenous auracyanin (Ac) from *Roseiflexus castenholzii* was
602 carried out by the methods as described (Wang et al., 2020). Before the oxidation assay, the
603 purified Ac was treated with sodium dithionite to obtain the reduced Ac. Using the reduced Ac
604 (122 μ M) as electron donor and varied concentrations of menaquinone-4 as electron acceptor, the
605 reaction was carried out in presence of nRC-LH or dRC-LH complex (50 nM) in buffer B (0.04 %
606 DDM, 100 mM NaCl, 50 mM Tris-HCl, pH 8.0). The reaction was initiated by illumination at
607 10,000 lux light intensity, and the absorbance of Ac at 604 nm was recorded by a UV-vis
608 spectrophotometer (Mapada P6, Shanghai) at 2 min intervals for a total of 14 min. The
609 corresponding concentrations of Ac were calculated with extinction coefficient, and linear initial
610 rates from 2 to 14 min were fitted using the Michaelis-Menten model in Prism8. All data were
611 obtained from three replicative experiments, with the mean and standard deviations calculated and
612 plotted.

613
614
615 **Data availability:** Cryo-EM maps and atomic coordinates of the native RC-LH (nRC-LH) and
616 carotenoid depleted RC-LH (dRC-LH) complexes extracted from cells grown under 10,000 lux
617 light intensity have been deposited into the Electron Microscopy Data Bank (accession codes,
618 EMD-34838 and EMD-34839) and the Protein Data Bank (PDB) (accession codes, 8HJU and
619 8HJV), respectively. Cryo-EM maps and atomic coordinates of the nRC-LH complexes extracted
620 from cells grown under 100 lux and 2,000 lux have been deposited into the Electron Microscopy
621 Data Bank (accession codes, EMD-35988 and EMD-35989) and the Protein Data Bank (PDB)

622 (accession codes, 8J5O and 8J5P), respectively. Other data are available from the corresponding
623 authors on reasonable request.

624

625

626

References

- 627 Adams, P. D., Afonine, P. V., Bunkoczi, G., Chen, V. B., Davis, I. W., Echols, N., Headd, J. J., Hung, L. W., Kapral,
628 G. J., Grosse-Kunstleve, R. W., McCoy, A. J., Moriarty, N. W., Oeffner, R., Read, R. J., Richardson, D. C.,
629 Richardson, J. S., Terwilliger, T. C., & Zwart, P. H. (2010). PHENIX: a comprehensive Python-based
630 system for macromolecular structure solution. *Acta Crystallogr D Biol Crystallogr*, *66*(Pt 2), 213-221.
631 doi:10.1107/S0907444909052925
- 632 Bramley, P. (1993). Inhibition of carotenoid biosynthesis. In *Carotenoids in photosynthesis* (pp. 127-159): Springer.
- 633 Cao, P., Bracun, L., Yamagata, A., Christianson, B. M., Negami, T., Zou, B., Terada, T., Canniffe, D. P., Shirouzu,
634 M., Li, M., & Liu, L. N. (2022). Structural basis for the assembly and quinone transport mechanisms of the
635 dimeric photosynthetic RC-LH1 supercomplex. *Nat Commun*, *13*(1), 1977. doi:10.1038/s41467-022-29563-
636 3
- 637 Collins, A. M., Qian, P., Tang, Q., Bocian, D. F., Hunter, C. N., & Blankenship, R. E. (2010). Light-harvesting
638 antenna system from the phototrophic bacterium *Roseiflexus castenholzii*. *Biochemistry*, *49*(35), 7524-7531.
639 doi:10.1021/bi101036t
- 640 Collins, A. M., Xin, Y., & Blankenship, R. E. (2009). Pigment organization in the photosynthetic apparatus of
641 *Roseiflexus castenholzii*. *Biochim Biophys Acta*, *1787*(8), 1050-1056. doi:10.1016/j.bbabbio.2009.02.027
- 642 Davidson, E., & Cogdell, R. J. (1981). Reconstitution of carotenoids into the light-harvesting pigment-protein
643 complex from the carotenoidless mutant of *Rhodospseudomonas sphaeroides* R26. *Biochim Biophys Acta*,
644 *635*(2), 295-303. doi:10.1016/0005-2728(81)90028-1
- 645 Emsley, P., & Cowtan, K. (2004). Coot: model-building tools for molecular graphics. *Acta Crystallogr D Biol*
646 *Crystallogr*, *60*(Pt 12 Pt 1), 2126-2132. doi:10.1107/S0907444904019158
- 647 Fiedor, L., Akahane, J., & Koyama, Y. (2004). Carotenoid-induced cooperative formation of bacterial photosynthetic
648 LH1 complex. *Biochemistry*, *43*(51), 16487-16496. doi:10.1021/bi0481287
- 649 Gall, A., Henry, S., Takaichi, S., Robert, B., & Cogdell, R. J. (2005). Preferential incorporation of coloured-
650 carotenoids occurs in the LH2 complexes from non-sulphur purple bacteria under carotenoid-limiting
651 conditions. *Photosynth Res*, *86*(1-2), 25-35. doi:10.1007/s11120-005-3481-0
- 652 Hanada, S., Takaichi, S., Matsuura, K., & Nakamura, K. (2002). *Roseiflexus castenholzii* gen. nov., sp. nov., a
653 thermophilic, filamentous, photosynthetic bacterium that lacks chlorosomes. *Int J Syst Evol Microbiol*, *52*(Pt
654 1), 187-193. doi:10.1099/00207713-52-1-187
- 655 Hashimoto, H., Uragami, C., & Cogdell, R. J. (2016). Carotenoids and Photosynthesis. *Subcell Biochem*, *79*, 111-
656 139. doi:10.1007/978-3-319-39126-7_4
- 657 Jackson, P. J., Hitchcock, A., Swainsbury, D. J. K., Qian, P., Martin, E. C., Farmer, D. A., Dickman, M. J., Canniffe,
658 D. P., & Hunter, C. N. (2018). Identification of protein W, the elusive sixth subunit of the
659 *Rhodospseudomonas palustris* reaction center-light harvesting 1 core complex. *Biochim Biophys Acta*
660 *Bioenerg*, *1859*(2), 119-128. doi:10.1016/j.bbabbio.2017.11.001
- 661 Kato, S., Masuda, S., Shibata, A., Shirasu, K., & Ohkuma, M. (2022). Insights into ecological roles of uncultivated
662 bacteria in Katase hot spring sediment from long-read metagenomics. *Front Microbiol*, *13*, 1045931.
663 doi:10.3389/fmicb.2022.1045931
- 664 Kishi, R., Imanishi, M., Kobayashi, M., Takenaka, S., Madigan, M. T., Wang-Otomo, Z. Y., & Kimura, Y. (2021).
665 Quinone transport in the closed light-harvesting 1 reaction center complex from the thermophilic purple
666 bacterium *Thermochromatium tepidum*. *Biochim Biophys Acta Bioenerg*, *1862*(1), 148307.
667 doi:10.1016/j.bbabbio.2020.148307
- 668 Kucukelbir, A., Sigworth, F. J., & Tagare, H. D. (2014). Quantifying the local resolution of cryo-EM density maps.
669 *Nat Methods*, *11*(1), 63-65. doi:10.1038/nmeth.2727

- 670 Lang, H., & Hunter, C. N. J. B. J. (1994). The relationship between carotenoid biosynthesis and the assembly of the
671 light-harvesting LH2 complex in *Rhodobacter sphaeroides*. *298*(1), 197-205.
- 672 Lang, H. P., Cogdell, R. J., Takaichi, S., & Hunter, C. N. (1995). Complete DNA sequence, specific Tn5 insertion
673 map, and gene assignment of the carotenoid biosynthesis pathway of *Rhodobacter sphaeroides*. *J Bacteriol*,
674 *177*(8), 2064-2073. doi:10.1128/jb.177.8.2064-2073.1995
- 675 McGlynn, P., Hunter, C. N., & Jones, M. R. (1994). The *Rhodobacter sphaeroides* PufX protein is not required for
676 photosynthetic competence in the absence of a light harvesting system. *FEBS Lett*, *349*(3), 349-353.
677 doi:10.1016/0014-5793(94)00701-2
- 678 Ng, I. W., Adams, P. G., Mothersole, D. J., Vasilev, C., Martin, E. C., Lang, H. P., Tucker, J. D., & Neil Hunter, C.
679 (2011). Carotenoids are essential for normal levels of dimerisation of the RC-LH1-PufX core complex of
680 *Rhodobacter sphaeroides*: characterisation of R-26 as a crtB (phytoene synthase) mutant. *Biochim Biophys*
681 *Acta*, *1807*(9), 1056-1063. doi:10.1016/j.bbabi.2011.05.020
- 682 Niwa, S., Yu, L. J., Takeda, K., Hirano, Y., Kawakami, T., Wang-Otomo, Z. Y., & Miki, K. (2014). Structure of the
683 LH1-RC complex from *Thermochromatium tepidum* at 3.0 Å. *Nature*, *508*(7495), 228-232.
684 doi:10.1038/nature13197
- 685 Olsen, J. D., Martin, E. C., & Hunter, C. N. (2017). The PufX quinone channel enables the light-harvesting 1 antenna
686 to bind more carotenoids for light collection and photoprotection. *FEBS Lett*, *591*(4), 573-580.
687 doi:10.1002/1873-3468.12575
- 688 Parkes-Loach, P. S., Sprinkle, J. R., & Loach, P. A. (1988). Reconstitution of the B873 light-harvesting complex of
689 *Rhodospirillum rubrum* from the separately isolated alpha- and beta-polypeptides and bacteriochlorophyll a.
690 *Biochemistry*, *27*(8), 2718-2727. doi:10.1021/bi00408a011
- 691 Pettersen, E. F., Goddard, T. D., Huang, C. C., Meng, E. C., Couch, G. S., Croll, T. I., Morris, J. H., & Ferrin, T. E.
692 (2021). UCSF ChimeraX: Structure visualization for researchers, educators, and developers. *Protein Sci*,
693 *30*(1), 70-82. doi:10.1002/pro.3943
- 694 Polivka, T., & Frank, H. A. (2010). Molecular factors controlling photosynthetic light harvesting by carotenoids. *Acc*
695 *Chem Res*, *43*(8), 1125-1134. doi:10.1021/ar100030m
- 696 Pugh, R. J., McGlynn, P., Jones, M. R., & Hunter, C. N. (1998). The LH1-RC core complex of *Rhodobacter*
697 *sphaeroides*: interaction between components, time-dependent assembly, and topology of the PufX protein.
698 *Biochim Biophys Acta*, *1366*(3), 301-316. doi:10.1016/s0005-2728(98)00131-5
- 699 Qian, P., Croll, T. I., Swainsbury, D. J. K., Castro-Hartmann, P., Moriarty, N. W., Sader, K., & Hunter, C. N. (2021).
700 Cryo-EM structure of the *Rhodospirillum rubrum* RC-LH1 complex at 2.5 Å. *Biochem J*, *478*(17), 3253-
701 3263. doi:10.1042/BCJ20210511
- 702 Qian, P., Gardiner, A. T., Simova, I., Naydenova, K., Croll, T. I., Jackson, P. J., Nupur, Kloz, M., Cubakova, P.,
703 Kuzma, M., Zeng, Y., Castro-Hartmann, P., van Knippenberg, B., Goldie, K. N., Kaftan, D., Hrouzek, P.,
704 Hajek, J., Agirre, J., Siebert, C. A., Bina, D., Sader, K., Stahlberg, H., Sobotka, R., Russo, C. J., Polivka, T.,
705 Hunter, C. N., & Koblizek, M. (2022). 2.4-Å structure of the double-ring Gemmatimonas phototrophica
706 photosystem. *Sci Adv*, *8*(7), eabk3139. doi:10.1126/sciadv.abk3139
- 707 Qian, P., Hunter, C. N., & Bullough, P. A. (2005). The 8.5Å projection structure of the core RC-LH1-PufX dimer of
708 *Rhodobacter sphaeroides*. *J Mol Biol*, *349*(5), 948-960. doi:10.1016/j.jmb.2005.04.032
- 709 Qian, P., Siebert, C. A., Wang, P., Canniffe, D. P., & Hunter, C. N. (2018). Cryo-EM structure of the *Blastochloris*
710 *viridis* LH1-RC complex at 2.9 Å. *Nature*, *556*(7700), 203-208. doi:10.1038/s41586-018-0014-5
- 711 Qian, P., Swainsbury, D. J. K., Croll, T. I., Castro-Hartmann, P., Divitini, G., Sader, K., & Hunter, C. N. (2021).
712 Cryo-EM Structure of the *Rhodobacter sphaeroides* Light-Harvesting 2 Complex at 2.1 Å. *Biochemistry*,
713 *60*(44), 3302-3314. doi:10.1021/acs.biochem.1c00576
- 714 Qian, P., Swainsbury, D. J. K., Croll, T. I., Salisbury, J. H., Martin, E. C., Jackson, P. J., Hitchcock, A., Castro-
715 Hartmann, P., Sader, K., & Hunter, C. N. (2021). Cryo-EM structure of the monomeric *Rhodobacter*
716 *sphaeroides* RC-LH1 core complex at 2.5 Å. *Biochem J*, *478*(20), 3775-3790. doi:10.1042/BCJ20210631
- 717 Sener, M., Strumpfer, J., Hsin, J., Chandler, D., Scheuring, S., Hunter, C. N., & Schulten, K. (2011). Forster energy
718 transfer theory as reflected in the structures of photosynthetic light-harvesting systems. *Chemphyschem*,
719 *12*(3), 518-531. doi:10.1002/cphc.201000944
- 720 Swainsbury, D. J. K., Qian, P., Jackson, P. J., Faries, K. M., Niedzwiedzki, D. M., Martin, E. C., Farmer, D. A.,
721 Malone, L. A., Thompson, R. F., Ranson, N. A., Canniffe, D. P., Dickman, M. J., Holten, D., Kirmaier, C.,

- 722 Hitchcock, A., & Hunter, C. N. (2021). Structures of Rhodospseudomonas palustris RC-LH1 complexes with
723 open or closed quinone channels. *Sci Adv*, 7(3). doi:10.1126/sciadv.abe2631
- 724 Tani, K., Kanno, R., Ji, X. C., Hall, M., Yu, L. J., Kimura, Y., Madigan, M. T., Mizoguchi, A., Humbel, B. M., &
725 Wang-Otomo, Z. Y. (2021). Cryo-EM Structure of the Photosynthetic LH1-RC Complex from
726 Rhodospirillum rubrum. *Biochemistry*. doi:10.1021/acs.biochem.1c00360
- 727 Tani, K., Kanno, R., Kikuchi, R., Kawamura, S., Nagashima, K. V. P., Hall, M., Takahashi, A., Yu, L. J., Kimura, Y.,
728 Madigan, M. T., Mizoguchi, A., Humbel, B. M., & Wang-Otomo, Z. Y. (2022). Asymmetric structure of the
729 native Rhodobacter sphaeroides dimeric LH1-RC complex. *Nat Commun*, 13(1), 1904. doi:10.1038/s41467-
730 022-29453-8
- 731 Tani, K., Kanno, R., Kurosawa, K., Takaichi, S., Nagashima, K. V. P., Hall, M., Yu, L. J., Kimura, Y., Madigan, M.
732 T., Mizoguchi, A., Humbel, B. M., & Wang-Otomo, Z. Y. (2022). An LH1-RC photocomplex from an
733 extremophilic phototroph provides insight into origins of two photosynthesis proteins. *Commun Biol*, 5(1),
734 1197. doi:10.1038/s42003-022-04174-2
- 735 Tani, K., Nagashima, K. V. P., Kanno, R., Kawamura, S., Kikuchi, R., Hall, M., Yu, L. J., Kimura, Y., Madigan, M.
736 T., Mizoguchi, A., Humbel, B. M., & Wang-Otomo, Z. Y. (2021). A previously unrecognized membrane
737 protein in the Rhodobacter sphaeroides LH1-RC photocomplex. *Nat Commun*, 12(1), 6300.
738 doi:10.1038/s41467-021-26561-9
- 739 Walz, T., & Ghosh, R. (1997). Two-dimensional crystallization of the light-harvesting I-reaction centre photounit
740 from Rhodospirillum rubrum. *J Mol Biol*, 265(2), 107-111. doi:10.1006/jmbi.1996.0714
- 741 Wang, C., Xin, Y., Min, Z., Qi, J., Zhang, C., & Xu, X. (2020). Structural basis underlying the electron transfer
742 features of a blue copper protein auracyanin from the photosynthetic bacterium Roseiflexus castenholzii.
743 *Photosynth Res*, 143(3), 301-314. doi:10.1007/s11120-020-00709-y
- 744 Xin, Y., Pan, J., Collins, A. M., Lin, S., & Blankenship, R. E. (2012). Excitation energy transfer and trapping
745 dynamics in the core complex of the filamentous photosynthetic bacterium Roseiflexus castenholzii.
746 *Photosynth Res*, 111(1-2), 149-156. doi:10.1007/s11120-011-9669-6
- 747 Xin, Y., Shi, Y., Niu, T., Wang, Q., Niu, W., Huang, X., Ding, W., Yang, L., Blankenship, R. E., Xu, X., & Sun, F.
748 (2018). Cryo-EM structure of the RC-LH core complex from an early branching photosynthetic prokaryote.
749 *Nat Commun*, 9(1), 1568. doi:10.1038/s41467-018-03881-x
- 750 Yamada, M., Zhang, H., Hanada, S., Nagashima, K. V., Shimada, K., & Matsuura, K. (2005). Structural and
751 spectroscopic properties of a reaction center complex from the chlorosome-lacking filamentous anoxygenic
752 phototrophic bacterium Roseiflexus castenholzii. *J Bacteriol*, 187(5), 1702-1709.
753 doi:10.1128/JB.187.5.1702-1709.2005
- 754 Yu, L. J., Suga, M., Wang-Otomo, Z. Y., & Shen, J. R. (2018a). Novel features of LH1-RC from Thermochromatium
755 tepidum revealed from its atomic resolution structure. *FEBS J*, 285(23), 4359-4366. doi:10.1111/febs.14679
- 756 Yu, L. J., Suga, M., Wang-Otomo, Z. Y., & Shen, J. R. (2018b). Structure of photosynthetic LH1-RC supercomplex
757 at 1.9 Å resolution. *Nature*, 556(7700), 209-213. doi:10.1038/s41586-018-0002-9
- 758 Zhang, K. (2016). Gctf: Real-time CTF determination and correction. *J Struct Biol*, 193(1), 1-12.
759 doi:10.1016/j.jsb.2015.11.003
- 760 Zheng, S. Q., Palovcak, E., Armache, J. P., Verba, K. A., Cheng, Y., & Agard, D. A. (2017). MotionCor2:
761 anisotropic correction of beam-induced motion for improved cryo-electron microscopy. *Nat Methods*, 14(4),
762 331-332. doi:10.1038/nmeth.4193
- 763 Zivanov, J., Nakane, T., Forsberg, B. O., Kimanius, D., Hagen, W. J., Lindahl, E., & Scheres, S. H. (2018). New
764 tools for automated high-resolution cryo-EM structure determination in RELION-3. *Elife*, 7.
765 doi:10.7554/eLife.42166

766

767

768

769

Acknowledgments

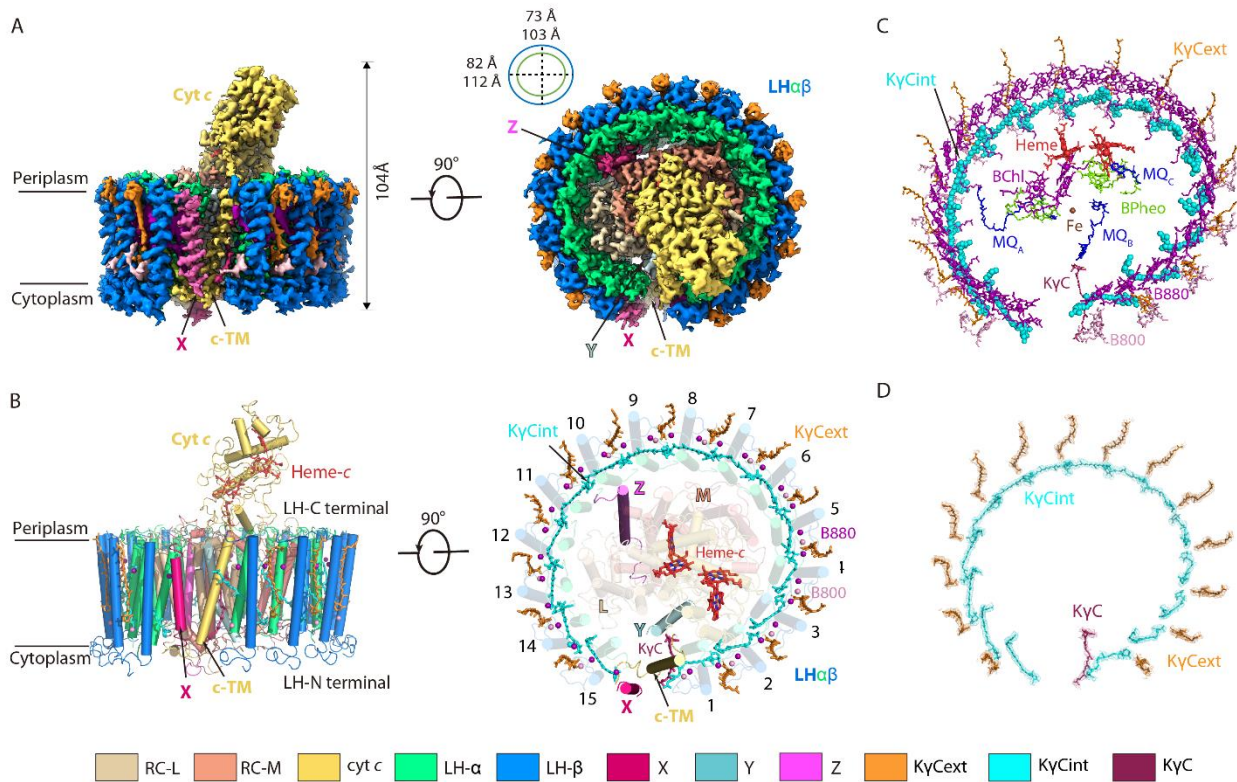
770 We thank Professor Fei Sun at the Institute of Biophysics, Chinese Academy of Science, and
771 Professor Weimin Ma at Shanghai Normal University for helpful discussions. We thank Danyu
772 Gu from the Instrumentation and Service Center for Molecular Sciences at Westlake University
773 for the assistance in measurement and data interpretation of the steady-state spectroscopic
774 analyses. We appreciate the help from Prof. Kezhi Jiang of Hangzhou Normal University for the
775 HPLC analysis of pigments. We thank the staff members of the Electron Microscopy System at
776 the National Facility for Protein Science in Shanghai (NFPS), Zhangjiang Lab, China for
777 providing technical support and assistance in data collection of the carotenoid depleted RC-LH
778 complex. We also thank Shuimu BioSciences Ltd. for the support of cryo-EM data collection for
779 the native RC-LH complex.

780 **Funding:** This work was supported by grants from the National Natural Science Foundation of
781 China (31870740, 32171227, 31570738), Zhejiang Provincial Natural Science Foundation of
782 China under Grant No. LR22C020002 to X. L. X. and Zhejiang Provincial Education Department
783 under Grant No. Y202044875 to J. Y. X.

784 **Author contributions:** X. L. X. initiated the project and supervised all experiments. J. Y. X.
785 purified and determined the cryo-EM structures of both the native and carotenoid depleted RC-
786 LH complexes from *Roseiflexus castenholzii*, and performed the steady-state spectroscopic
787 analyses. Y. S. assigned the subunit X, protein Y and Z in the RC-LH complex. X. Z. assisted in
788 cryo-EM sample preparation and data processing. X. Y. Y. and H. M. H. performed the HPLC
789 and LC-MS analyses of the pigments. Y. Y. X. and J. J. S. assisted in the spectral and enzymatic
790 characterizations of the RC-LH complexes. X. L. X., R. E. B and J. Y. X. analyzed the data and
791 wrote the manuscript.

792
793 **Competing interests:** The authors declare no conflict of interest.
794
795

796 **Figures**



798

799 **Figure 1. Overall structure of the native reaction center (RC)-light harvesting (LH) complex**

800 **from *Roseiflexus castenholzii*.** (A) A cryo-EM map of the native RC-LH (nRC-LH) complex is

801 shown from the side (left panel) and the bottom (right panel). The dimensions of the RC-LH

802 complex and LH ring are represented. The positions of subunit X, proteins Y and Z, and the

803 cytochrome (cyt) *c* transmembrane domain (c-TM) are labeled. (B) Side and top views of the

804 nRC-LH complex are presented in cartoon form. LH subunits are numbered clockwise from the

805 gap formed by subunit X and c-TM. Heme-*c* (red) and keto- γ -carotene molecules (orange, cyan,

806 ruby) are shown in stick forms; Mg atoms of the bacteriochlorophylls B800 (pink) and B880

807 (purple) are shown as spheres. (C) The cofactors bound in the nRC-LH complex. All cofactors are

808 shown in stick forms except for the interior keto- γ -carotenes (K γ C_{int}) in LH, the iron bound in the

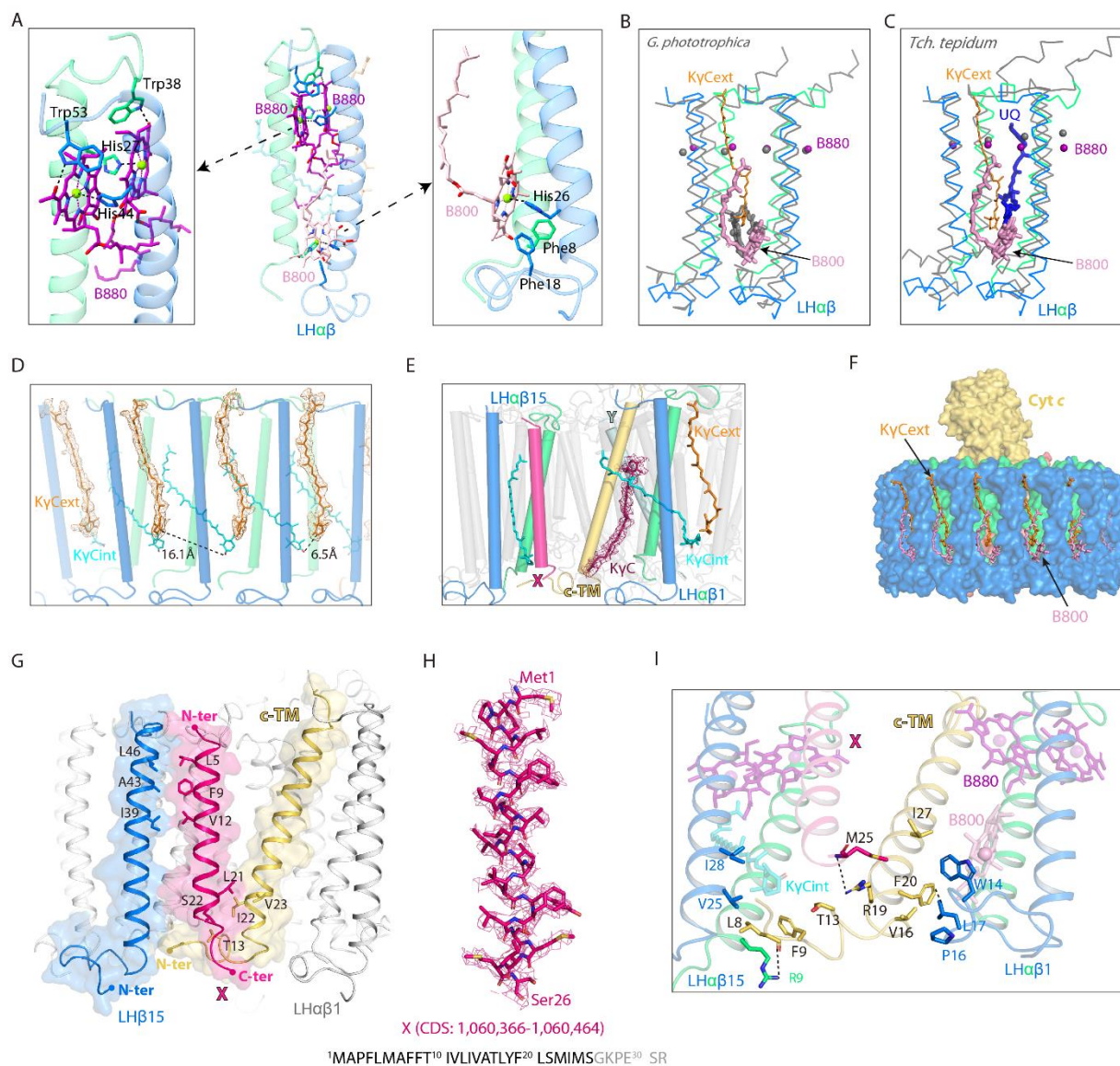
809 RC are shown as spheres. (D) The structural models of the interior keto- γ -carotenes (K γ C_{int}),

810 exterior keto- γ -carotenes (K γ C_{ext}) and K γ C in the nRC-LH complex are fitted in the EM density

811 map. The color scheme: Lime green, α -polypeptides; marine, β -polypeptides; yellow-orange, cyt *c*;

812 wheat, L subunit; salmon, M subunit; pale cyan, protein Y; hot pink, subunit X; light magenta,
 813 protein Z; cyan, $K\gamma C_{int}$; orange, $K\gamma C_{ext}$; ruby, $K\gamma C$; Purple, B880; pink, B800; tv-red, heme-*c*;
 814 chartreuse, BPh eos; blue, menaquinone-11 (MQ); brown, iron.

815



816

817 **Figure 2. Interactions of the keto- γ -carotenes, BChls, and subunit X with the light**

818 **harvesting (LH) ring. (A) Interactions between the LH $\alpha\beta$ heterodimer and the bound BChls.**

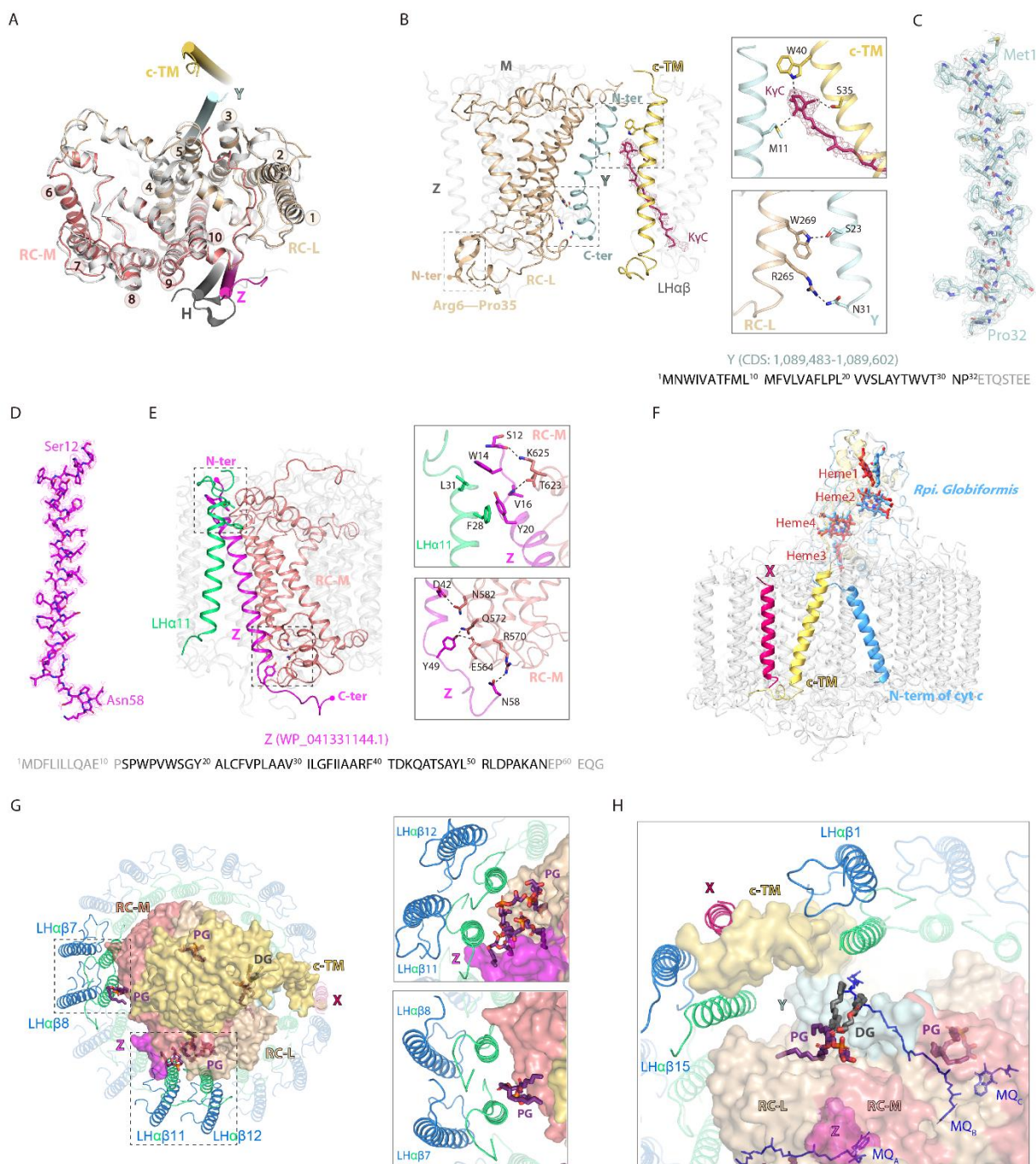
819 **Close-up views of amino acid residues that coordinate the LH-bound B880s and B800**

820 **(right) are shown on the two sides. The BChls and interacting amino acid residues are shown in**

821 **stick forms. (B, C) Superposition of LH $\alpha\beta$ heterodimer from nRC-LH (colored) with**

822 *Gemmatimonas (G.) phototrophica* LHh (B, gray) and *Thermochromatium (Tch.) tepidum* LH1
823 (C, gray). The LH-bound B800 and exterior keto- γ -carotenes ($K\gamma C_{ext}$) in nRC-LH are shown as
824 pink and orange sticks, respectively. Mg atoms of LH-bound B880 are shown in spheres. The
825 LHh-bound B800 in *G. phototrophica* is shown in gray sticks, and *Tch. tepidum* LH1-bound
826 ubiquinone (UQ) is shown in blue sticks. **(D, E)** Keto- γ -carotene organization. Interior keto- γ -
827 carotenes ($K\gamma C_{int}$) are shown in cyan, exterior keto- γ -carotenes ($K\gamma C_{ext}$) are shown in orange, and
828 the $K\gamma C$ inserted between c-TM and LH $\alpha\beta$ is shown in ruby. **(F)** Incorporation of the $K\gamma C_{ext}$ and
829 B800s at the cytoplasmic side blocked the LH $\alpha\beta$ interface. **(G, I)** Interactions between the
830 assigned subunit X (hot pink), c-TM (yellow-orange), and neighboring LH $\alpha\beta$ 1 and LH $\alpha\beta$ 15 in the
831 nRC-LH. The N-terminus (N-ter) and C-terminus (C-ter) of subunit X, c-TM and LH β 15 are
832 indicated. The hydrogen bonding and hydrophobic interactions between the amino acid residues
833 are labeled and indicated with dashed lines. The BChls B880 and B800 are shown as purple and
834 pink sticks, respectively. **(H)** The assigned subunit X (hot pink) are fitted in the EM density map.
835 Location of the coding sequence (CDS) in *R. castenholzii* genomic DNA, and the amino acid
836 sequence of subunit X are indicated, with the modeled amino acid residues colored in black.

837



838

839

840

Figure 3. Stabilizing the reaction center (RC)-light harvesting (LH) interactions. (A)

841

Superposition of *R. castenholzii* RC structure (colored) with that of *Rhodobacter* (*Rba.*)

842

sphaeroides (white, PDB ID: 7F0L) showed excellent match at the L (wheat) and M (salmon)

843

subunits, each of which contains five transmembrane helices (TM1-5 for L, and TM-6-10 for M).

844

The newly assigned TM helices from protein Y (pale cyan) and Z (light magenta) are located on

845

the two sides of the RC. The only TM helix of *Rba.* sphaeroides H subunit (gray) does not match

846 with that of protein Z. **(B)** Interactions between the assigned protein Y (pale cyan), c-TM (yellow-
847 orange), and the RC-L (wheat). The N-terminus (N-ter) and C-terminus (C-ter) of Y, and RC-L
848 N-terminal extension (Arg6-Pro35) are indicated. The hydrogen bonding interactions between the
849 amino acid residues and K γ C (ruby sticks) are labeled and indicated with dashed lines in the
850 insects. **(C, D)** The assigned TM helix of protein Y (C, pale cyan) and protein Z (D, light
851 magenta) are fitted in the EM density map. Location of the coding sequence (CDS) of Y in R.
852 castenholzii genomic DNA, and the protein accession number of protein Z are indicated. The
853 amino acid sequences of protein Y and Z are indicated below, with the modeled amino acid
854 residues colored in black. **(E)** Interactions between the assigned protein Z (light magenta), LH α 11
855 (lime green), and the RC-M (salmon). The N-terminus (N-ter) and C-terminus (C-ter) of Z are
856 indicated. The hydrogen bonding interactions are shown in the insects. **(F)** Superposition of R.
857 castenholzii RC-bound cyt c (yellow-orange) with that of Rhodospila (Rpi.) Globiformis
858 (cornflower blue, PDB ID: 7XXF) showed excellent match at the tetra-heme binding domain. The
859 c-TM and N-ter of Rpi. Globiformis cyt c directed into opposite directions. **(G, H)** Interactions of
860 the lipids (phosphatidylglycerol, PG; and diglyceride, DG) with the LH and RC. The L, M and cyt
861 c subunits of RC are shown in surface, and LH $\alpha\beta$ s are shown in cartoon forms, the lipids and RC-
862 bound menaquinone-11s (MQs) are shown in deep purple and blue sticks, respectively.

863

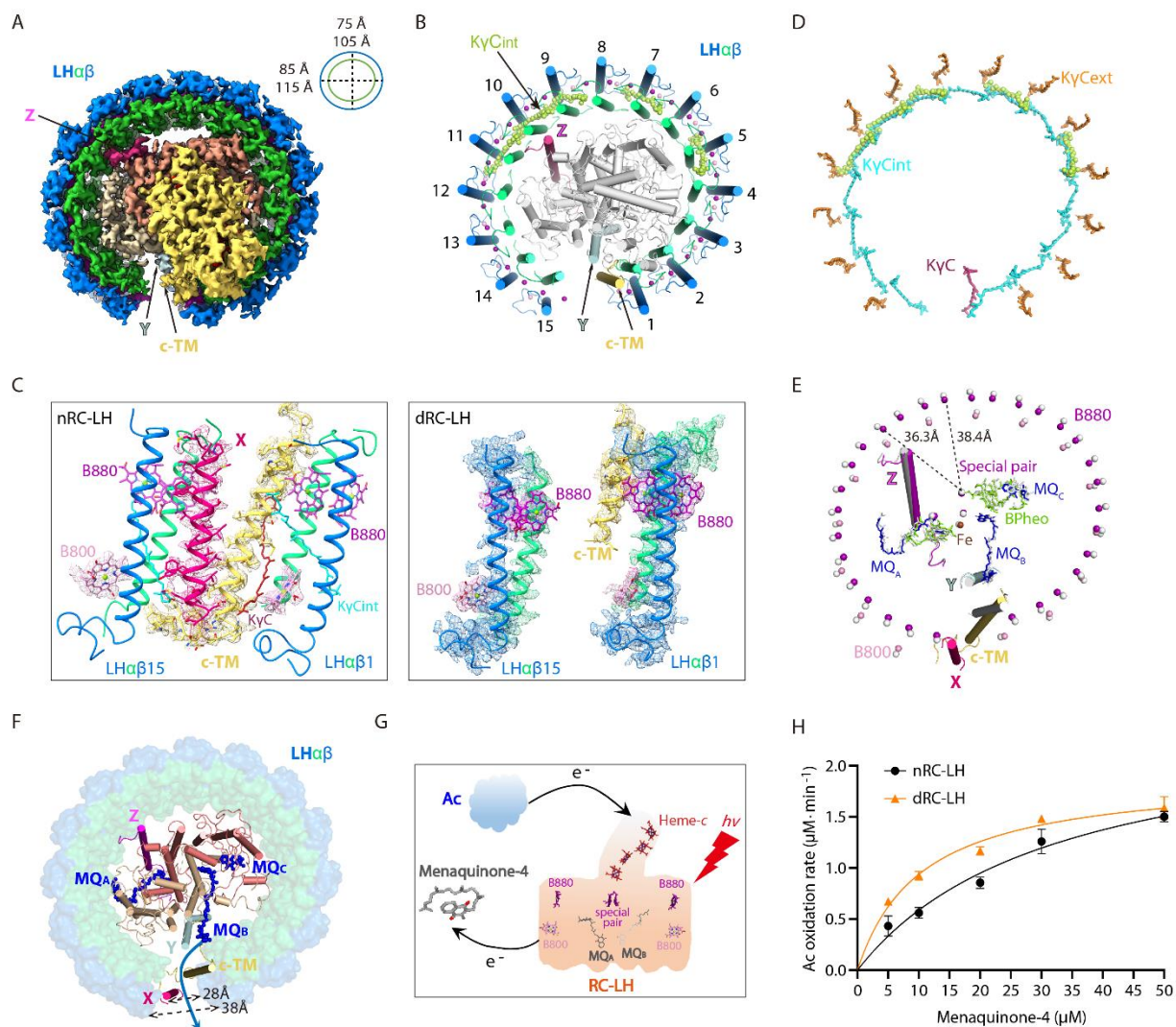


Figure 4 Cryo-EM structure of the carotenoid reaction center-light harvesting

(dRC-LH) complex of *Roseiflexus castenholzii* and its conformational changes that

accelerated quinone/quinol exchange. (A) Cryo-EM map of dRC-LH seen from the bottom with

LH ring dimensions indicated. (B) Cartoon representation of the dRC-LH complex from the

bottom. The interior keto- γ -carotenes ($K\gamma C_{int}$) are shown in limon and bacteriochlorophyll (BChl)

Mg atoms are shown as spheres. (C) Comparison of the LH ring openings in the nRC-LH (left)

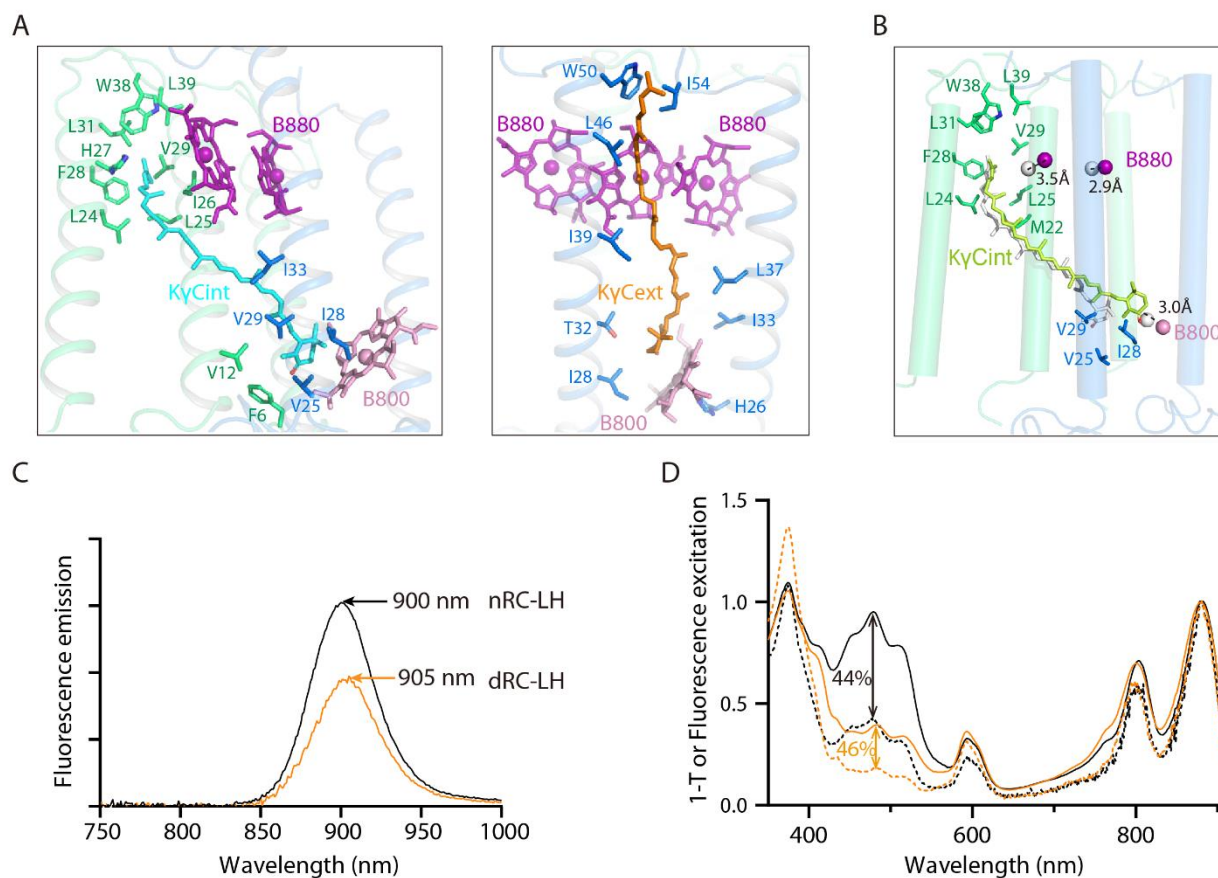
and dRC-LH (right). The cryo-EM maps of the subunit X (hot pink), c-TM (yellow-orange) and

neighboring LH $\alpha\beta$ 1 and LH $\alpha\beta$ 15 are shown to indicate the conformational changes. The LH-

bound B880s (purple), B800s (pink) and $K\gamma C$ (ruby) are shown in sticks and fitted in the EM

map. (D) Comparison of the keto- γ -carotene arrangement between the nRC-LH and dRC-LH

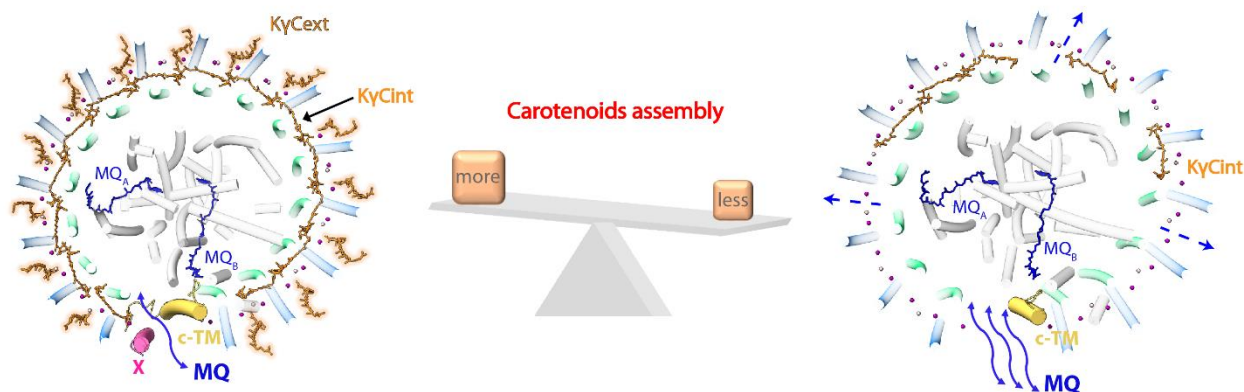
875 complexes. The $K\gamma C_{int}$, $K\gamma C_{ext}$ and $K\gamma C$ in nRC-LH are shown as cyan, orange and ruby sticks,
876 respectively. The five $K\gamma C_{int}$ molecules bound in the dRC-LH complex are shown as limon
877 spheres. **(E)** Comparison of the central BChl-Mg atoms in nRC-LH and dRC-LH. The B880 and
878 B800 Mg atoms are shown as purple and pink spheres, respectively, in nRC-LH, and as white
879 spheres in dRC-LH. The two structures are superposed at the TM helices of the L and M subunits.
880 The distances between the central Mg atoms of B880 and the nearest special pair BChls are
881 labeled and indicated with dashed lines. The cofactors bound in the RC are shown in stick form;
882 the iron is shown as spheres. TM helices of Subunit X (hot pink), protein Y (pale cyan), Z (light
883 magenta), c-TM (yellow-orange in nRC-LH and white in dRC-LH), and $LH\alpha\beta 1$ and $LH\alpha\beta 15$
884 (colored in nRC-LH and white in dRC-LH) are shown in ribbon form to demonstrate the spatial
885 organization. **(F)** Comparison of the LH ring opening and quinone channels in nRC-LH and dRC-
886 LH. The LH ring of dRC-LH is shown in surface form; the RC (including Y and Z), c-TM, and
887 subunit X in nRC-LH are shown in cartoon forms; and menaquinones (MQs) are shown in blue
888 sticks. Dashed lines indicate the dimensions of the LH ring openings in the two structures. The
889 blue arrow represents the putative quinone shuttling path. **(G)** Model diagram of the auracyanin
890 (Ac) oxidation assay. Upon illumination, light energy absorbed by the LH-bound BChls (B800
891 and B880) is transferred to RC. The primary charge separation occurs and initiates sequential
892 electron transfer that reduces the MQs. The generated hydroquinone diffuses out of the RC-LH
893 and exchanges with the menaquinone-4 in the solution. Once the reduced Ac is oxidized, the
894 released electrons can be transferred back to reduce the photo-oxidized special pair through the c-
895 type hemes. **(H)** The rate of auracyanin (Ac) oxidation at various starting concentrations of
896 menaquinone-4, in presence of the nRC-LH (black) or dRC-LH (orange).



897
898 **Figure 5 Binding conformation of the interior and exterior keto- γ -carotenes ($K\gamma C_{int}$ and**
899 **$K\gamma C_{ext}$, respectively) and measurement of the Car-to-BChl energy transfer efficiency in**
900 **nRC-LH and dRC-LH complexes. (A) Coordination of representative $K\gamma C_{int}$ (cyan) and $K\gamma C_{ext}$**
901 **(orange) molecules in the nRC-LH complex. Shown as stick forms are the amino acid residues**
902 **from LH α (lime green) and LH β (marine) surrounding the 4-oxo- β -ionone ring; the ψ -end group**
903 **of the keto- γ -carotenes; and the BChls B880 (purple) and B800 (pink) in the nearby LH $\alpha\beta$. (B)**
904 **Coordination of the $K\gamma C_{int}$ molecules, which are shown in limon and white in dRC-LH and nRC-**
905 **LH, respectively. Amino acid residues from the nearby LH α (lime green) and LH β (marine) and**
906 **the B800 molecule that covers the head and tail of this $K\gamma C_{int}$ molecule are shown as stick forms.**
907 **The distance deviations of the central Mg atoms in B880 (purple) and B800 (pink) in the two**
908 **structures are labeled and indicated with dashed lines. (C) Spectral analysis of the RC-LH**
909 **complex. Fluorescence emissions are shown for nRC-LH (black) and dRC-LH (orange)**
910 **complexes isolated from *Roseiflexus castenholzii* after excitation at 470 nm. (D) Fluorescence**

911 excitation and absorption (1-T) spectra are shown as dotted and solid lines, respectively, for
912 nRC-LH (black) and dRC-LH (orange). The Car-to-BChl energy transfer efficiency (vertical
913 dashed line) was calculated by normalizing the fluorescence excitation and absorption spectra at
914 880 nm to 1.0.

915



916

917 **Figure 6 Schematic diagram of the carotenoid (Car) assembly related structural dynamics**

918 **of *Roseiflexus castenholzii* RC-LH complex.** In native RC-LH, incorporation of the external

919 keto- γ -carotenes (K γ C_{ext}) and LH-bound B800s blocked the LH $\alpha\beta$ interface. Alternatively, the

920 subunit X disrupts the ring and forms a potential quinone channel with the c-TM, facilitating

921 controlled quinone/quinol binding and shuttling. In dRC-LH, less carotenoid (Car) assembly

922 exposed the LH $\alpha\beta$ interface, absence of the subunit X and cytoplasmic region of c-TM

923 concomitantly broadened the LH opening, which together accelerated the quinone/quinol

924 exchange.

925